Synergistic Fatigue Performance in High Entropy Alloys with Novel Precipitates and Metastable Phases

A Dissertation Presented for the
Doctor of Philosophy
Degree
The University of Tennessee, Knoxville

Zongyang Lyu
May 2023

DEDICATION

This doctoral dissertation is dedicated to my parents, my wife, and all beloved ones for offering the most unconditional supports.

ACKNOWLEDGEMENTS

Firstly, I would like to appreciate the support and guidance from my advisors, Prof. Peter Liaw and Prof. Yanfei Gao. It is also my great honor to have Prof. Hahn Choo, Prof. Katharine Page, and Prof. Chad Duty.

I would like to express my thanks to Dr. Ke An, Dr. Yan Chen, Dr. Dunji Yu from Oak Ridge National Laboratory (ORNL) for the help on in situ neutron diffraction tests at VULCAN of Spallation Neutron Source (SNS). My thanks also go to Dr. Jonathan Poplawsky for the help on atomic probe tomography (APT) characterizations at ORNL. I am grateful to Prof. Huamiao Wang from Shanghai Jiaotong University (SJTU) and Dr. Tongde Shen from Yanshan University for the help on self-consistent modeling and material preparation, respectively.

I appreciate all the help from my student colleagues, Dr. Rui Feng, Dr. Di Xie, Mr. Xuesong Fan, Ms. Amalia Lia, Mr. Hugh Shortt, and Mr. John Whitlow.

I would like to acknowledge the financial support from the National Science Foundation grant of DMR-1611180 and DMR-1809640. I also thank for the support from Center for Materials Processing.

ABSTRACT

Recently, a new concept of the alloying-design strategy, called high-entropy alloys (HEAs), has been developed. Unlike traditional alloys based on one element as the principal component, HEAs are designed with four or more principal elements. The HEAs have been regarded as promising alloys with excellent mechanical properties. However, most of the investigations focused on the tensile or compressive behaviors and the fatigue properties of HEAs are still not well studied. The goal of our proposed research is to investigate the low cycle fatigue behaviors of HEAs and try to explore the stronger HEAs with excellent fatigue resistance by introducing multicomponent nanosized precipitates and phase transformations. The combination of the in-situ diffraction techniques and micromechanical models is used to establish the relationship between macroscopic properties and microstructural mechanisms during low cycle fatigue tests. This investigation could accelerate the engineering applications of HEAs.

TABLE OF CONTENTS

LIST OF TABLES

LIST OF FIGURES

CHAPTER 1. INTRODUCTION

A new concept of the alloying-design strategy, called high-entropy alloys (HEAs), has been developed in recent years. Unlike the traditional alloys based on one element as the principal component, HEAs are designed with four or more principal elements with the concentration between 5 and 35 atomic percentages [1-3]. There is another definition which is based on the concept of configurational entropy, i.e., HEAs are alloys having configurational entropies in the random state, larger than 1.5R, where R is the ideal gas constant, no matter a single-phase or multi-phase alloy forms at room temperature [4].
There are several other names for HEAs, such as baseless alloys (BAs), multi-principal element alloys (MPEAs), complex concentrated alloys (CCAs), compositionally complex alloys (CCAs), and metal buffets (MBs), which focus on the wide range of compositional space instead of the scale of entropy or the types of phases [5-8].

The HEAs have been reported to have excellent mechanical properties [2, 9-18]. For example, the CrMnFeCoNi HEA exhibits higher fracture toughness than most pure metals and metallic alloys and possesses a strength comparable to that of structural ceramics and close to that of some bulk metallic glasses [11]. In the oxygen- and the nitrogen-doped TiZrHfNb HEAs, the yield strength increases from 0.75 ± 0.03 GPa for the base HEA to 1.11 ± 0.03 and 1.30 ± 0.02 GPa, while the elongation has nearly doubled, increasing from 14.21% ± 1.09% for the base HEA to 27.66% ± 1.13% for the oxygen-doped HEA [10]. The HEAs are promising structural materials for future practical applications. The $Al_{0.5}CoCrCuFeNi$ HEA [12, 19] show promising high cycle fatigue resistance, which has higher fatigue ratio (fatigue-endurance limit/ultimate tensile strength) than other metallic materials with respect to the ultimate tensile strengths (UTS). The $Al_{0.5}CoCrFeNi$ HEA was reported to possess excellent low cycle fatigue performance at low strain amplitudes due to the high elasticity, plastic deformability, and martensitic transformation of the B2 phase [18].

1.1 Motivation and Objective

It is a core topic to seek for stronger alloys with excellent fatigue properties for our industrial applications. However, the fatigue properties of HEAs have not be well studied. The goal of our proposed research is to investigate the fatigue behaviors of HEAs and try to explore the stronger HEAs with excellent fatigue resistance. This investigation could accelerate the engineering application of HEAs. Previous studies on fatigue behaviors are mainly based on the ex-situ characterizations, such as scanning electron microscope (SEM), electron backscatter diffraction (EBSD), and transmission electron microscope (TEM). The novelty of this work is to use the non-destructive in-situ diffraction techniques coupled with micromechanical models to establish the relationship between macroscopic properties and microstructural mechanisms during fatigue tests.

1.2 Framework

There are three tasks for this proposed work. Task1 is mechanical behavior of Al0.3CoCrFeNi high-entropy alloy under low-cycle fatigue. Task2 is mechanical behavior of multicomponent intermetallic nanoparticle strengthened high-entropy alloy under low-cycle fatigue. Task3 is Mechanical behavior of metastable high-entropy alloy under low-cycle fatigue. For the study of LCF behavior, it is very important to conduct the in-situ, real-time study, since the twinning or phase transformation may happen during the loading condition and vanish during the ex-situ/unloading condition. In order to achieve our tasks, in-situ diffraction techniques are used to help building up more accurate and quantitative analysis of the deformation behaviors of HEAs under fully reversed LCF. Coupled with micromechanical models, we can establish the relationship between macroscopic properties and microstructural mechanisms. The overall framework is shown in the Figure 1.

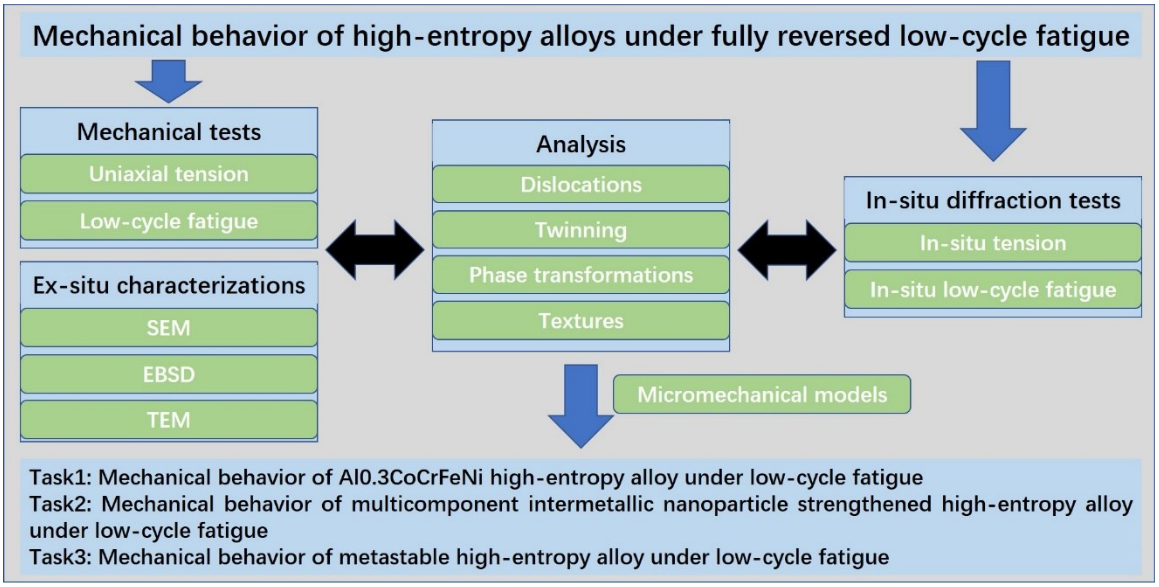

Figure 1. Overall framework of the proposed work.

CHAPTER 2.
LOW CYCLE FATIGUE PERFORMANCES OF AL0.3COCRFENI HIGH ENTROPY ALLOYS: IN SITU NEUTRON DIFFRACTION STUDIES ON THE PRECIPITATION EFFECTS

Abstract

Fatigue properties are essential for structural materials in industrial applications. High-entropy alloys are promising fatigue resistant alloys with high strengths and good performance in other mechanical properties. The B2 precipitate could significantly strengthen the yield strength of the $Al_{0.3}CoCrFeNi$ high-entropy alloy, however, decrease the low-cycle fatigue life. The underlying deformation mechanisms is worth being investigated, which could provide insights into the precipitate effect on the FCC high-entropy alloys. Here, the $Al_{0.3}CoCrFeNi$ alloys with single face-centered-cubic (FCC) phase and with FCC + B2 phases are used for the investigation of the low-cycle fatigue behavior by real-time in situ neutron diffraction measurements and elastic-viscoplastic self-consistent modeling. The simulation results indicate that the B2 precipitates could highly increase the back stresses during cyclic loading by facilitating the kinematic hardening in the matrix, while the effect of dynamic recovery is relatively weak. Due to the highly increased tensile strength by the “hard” B2 precipitate, the “soft” FCC grain families need to take more plastic shear strains, which could promote the formation of persistent slip bands (PSBs) in the FCC phase. The promotion of the generation of PSBs and back stresses provide more fatigue-crack-initiation sites and thus the damage accumulation, which will further lead to the shorter fatigue life.

2.1 Introduction

High-entropy alloys (HEAs), also called multicomponent alloys, is a newly developed alloying strategy. Unlike the traditional alloys with one or two principal elements, HEAs have at least four principal elements and simple main phase structures, such as face-centered-cubic (FCC), body-centered-cubic (BCC), and hexagonal-close-packed (HCP) [1-3]. HEAs are proved to have high strength and ductility, as well as excellent fracture toughness [2, 9, 10, 17, 20-23]. However, most of the studies on HEAs are focused on the monotonic tension or compression tests. The understanding of fatigue behaviors of HEAs is still limited, especially for low-cycle fatigue (LCF).

The most well-known HEA (Cantor alloy), CoCrFeMnNi, has been investigated for the LCF property [24-26]. The CoCrFeMnNi alloy has similar fatigue-crack growth behavior to twinning-induced plasticity (TWIP) steel and the LCF life of CoCrFeMnNi is lower than that of TWIP steel at all strain amplitudes (0.85% - 0.3%), but higher than that of SS304 steel at high strain amplitudes (0.85% - 0.55%) [24]. Even though the LCF life is higher than that of SS304 steel at high strain amplitudes, the strength is still lower than that of other high-strength materials. Equal Channel Angular Pressing (ECAP) was conducted to increase the yield strength of the Cantor alloy by Picak et al. [25], and the cyclic response of both coarse and ultrafine grained Cantor alloys was investigated during LCF at room temperature. The ECAP sample exhibits greater fatigue life of the CoCrFeMnNi HEA at the lowest strain amplitude of 0.2%. However, the hot-extruded sample has better fatigue life at the highest strain amplitude of 0.6% [25]. The grain-size effect on LCF of a carbon-containing CoCrFeMnNi HEA was investigated by Shams et al. [26], and the fatigue life of warm-rolled and annealed samples with small grain sizes was increased at low total strain amplitudes (0.4% and 0.55%), which is attributed to an increase in the elastic resistance owing to the higher strength of the fine-grained HEA than the coarse-grained HEA. Besides the investigations on the Cantor alloy, the ductile-transformable multicomponent B2 precipitates can be used to enhance the fatigue life of the $Al_{0.5}CoCrFeNi$ HEA, as well as the strength. Feng et al. [18] found that the $Al_{0.5}CoCrFeNi$ HEA with a ductile-transformable multicomponent B2 exhibits at least four times longer life than conventional alloys at the plastic strain amplitude of ~ 0.03% and maintains comparable LCF properties with traditional alloys at high strain levels. The fine ductile-transformable B2 phase could hinder the initiation of microcracks because of stress relaxation and strain partitioning during plastic deformation and martensitic transformation, which facilitate the relief of cyclic damage accumulation caused by the deformation incompatibility between the B2 and FCC phases [18]. In this case, the precipitate can enhance both the strength and LCF resistance. In addition, some research showed that the coherent precipitates in aluminum alloys are easily cut by dislocations and consequently lead to slip localization and early failure [27]. For alloys with two phases, the back stress generated from the “phase to phase” strain incompatibility, plastic strain incompatibilities, and heterogeneous plastic deformation could play an important role in the cyclic response during cyclic loading, such as the Ti-6Al-4V alloy [28].

In the present work, we investigated the LCF behavior of the $Al_{0.3}CoCrFeNi$ high-entropy alloy (denoted as Al0.3), and the Al0.3 with a single FCC phase has excellent LCF life at high strain amplitudes (> 1%). The Al0.3 with an FCC + B2 phase structure has also been studied for comparison. With the precipitate strengthening, the yield strength of Al0.3 nearly doubles while the LCF life becomes shorter, which could have different deformation mechanisms than the single phase Al0.3 alloy. The combination of in situ neutron diffraction and elastic-viscoplastic self-consistent (EVPSC) modeling are used in this work to study the LCF behavior of the $Al_{0.3}CoCrFeNi$ HEA. The deformation behaviors, such as lattice-strain evolutions, of different grain families of phases along the loading direction could be measured by the in situ neutron diffraction, which provide the input information for the EVPSC model simulations. The present research could assist us to have a better understanding of the incoherent precipitate effect on the FCC HEAs during LCF.

2.2 Experimental

2.2.1 Material Processing

The $Al_{0.3}CoCrFeNi$ HEA was fabricated by melting and casting into a plate. Then the plate was treated using hot-isostatic pressing (HIP) at 1,204 °C and 103 MPa for 4 h to reduce the casting defects. After that, there were two different heat treatments for the $Al_{0.3}CoCrFeNi$ HEA. One is the homogenization at 1,200 °C for 1 h, followed by water quenching for a single FCC phase. Another is annealed at 700 °C for 500 h after the 1,200 °C homogenization, followed by water quenching, for the FCC + B2 phase structure.

2.2.2 Mechanical Testing

The dog-bone samples with gauge dimensions of ϕ8mm $\times$ 16 mm were used for the low-cycle fatigue (LCF) test. The strain-controlled LCF tests were performed at room-temperature using an MTS Model 810 servo-hydraulic machine. The strain amplitudes are $\pm 1.5\%$, $\pm 1.25\%$, $\pm 1.0\%$, $\pm 0.75\%$, $\pm 0.5\%$, $\pm 0.35\%$, and $\pm 0.25\%$, respectively. The strain rate is $1 \times 10^{-2}\ s^{-1}$ and the initial loading is in tension.

2.2.3 Microstructural Characterizations

The microstructure was characterized by a Zeiss EVO scanning-electron microscope (SEM). The specimens for SEM were initially polished with the 1,200-grit SiC paper and then vibratorily polished with the 0.05 μm SiC suspension for the final surface polishing. The transmission electron microscope (TEM) was performed on a ZEISS LIBRA 200 HT FE MC. The TEM samples were prepared by twin-jet polishing with an electrolyte consisting of 95% ethanol and 5% perchloric acid in a volume fraction under −40 °C and voltage of 30 V.

2.2.4 In situ neutron Diffraction Measurement

The in situ LCF neutron-diffraction test was performed, using an MTS load frame at the VULCAN Engineering Materials Diffractometer [29, 30], the Spallation Neutron Source (SNS), Oak Ridge National Laboratory (ORNL). The fully-reversed strain-controlled LCF tests were conducted at different strain amplitudes with triangular loading waveforms under a continuous-loading condition. The strain amplitude was $\pm 1\%$, and the initial loading is in tension. The diffraction data were recorded with a strain rate of ~ $7 \times 10^{-6}\ s^{-1}$. The data of LCF will be collected at several selected cycles based on the lab results, such as 1st, 2nd, and 5th cycles. The in situ neutron diffraction data were analyzed, using the VULCAN Data Reduction and Interactive Visualization software (VDRIVE) [31]. The lattice strain of a given (hkl) plane is determined by:

$$\varepsilon_{hkl} = \frac{d_{hkl} - d_{hkl}^0}{d_{hkl}^0} \tag{1}$$

where $d_{hkl}^0$and d_{hkl} refer to lattice d-spacing in the stress-free condition and the lattice d-spacing during the loading condition, respectively.

The evolution of the dislocation density is investigated, using the relationship between the dislocation density of a certain lattice plane and its full width at half maximum (FWHM) of the diffraction peak described by the following equation [32, 33]:

$$\rho_{hkl} \propto \frac{FWHM_{G,hkl}^2}{d_{hkl}^2 b^2\, C_r} \tag{2}$$

where ρ is the density of randomly distributed dislocations, *hkl* is the Miller index, $\mathrm{FWHM}_{\mathrm{G,hkl}}$ is the Gaussian component of the FWHM of certain peak, *d* is the lattice-plane spacing, *b* is the magnitude of the Burgers vector, and C_r is the contrast factor associated with the dislocation character (edge or screw).

2.2.5 Elastic Visco-plastic Self-consistent Simulations

The collective deformation behavior of polycrystalline aggregates can be nicely modeled by the EVPSC model [18]. As for an individual grain, the total strain rate can be expressed as:

$$\dot{\boldsymbol{\varepsilon}} = \dot{\boldsymbol{\varepsilon}}^e + \dot{\boldsymbol{\varepsilon}}^p = \boldsymbol{M}^e : \dot{\boldsymbol{\sigma}} + \boldsymbol{M}^p : \boldsymbol{\sigma} + \dot{\boldsymbol{\varepsilon}}_0 \tag{3}$$

where $\dot{\boldsymbol{\varepsilon}}^e$ and $\dot{\boldsymbol{\varepsilon}}^p$ stand for the elastic strain rate and plastic strain rate, respectively. $\boldsymbol{M}^e$, $\boldsymbol{M}^p$, and $\dot{\boldsymbol{\varepsilon}}_0$ represent the elastic compliance, plastic compliance, and back-extrapolated strain rate, respectively. The macroscope strain rate has the similar formula and can be written as the follow equation:

$$\dot{\boldsymbol{E}} = \overline{\boldsymbol{M}}^{e} : \dot{\boldsymbol{\Sigma}} + \overline{\boldsymbol{M}}^{p} : \boldsymbol{\Sigma} + \dot{\boldsymbol{E}}_0 \tag{4}$$

where $\overline{\boldsymbol{M}}^{e}$, $\overline{\boldsymbol{M}}^{p}$, and $\dot{\boldsymbol{E}}_0$ are the elastic compliance, plastic compliance, and back-extrapolated strain rate for a homogeneous effective medium, respectively. An extended Voce law is applied to simulate the work-hardening behavior of the slip systems, as expressed by:

$$\hat{\tau}_{cr} = \tau_0 + (\tau_1 + h_1 \Gamma)\left\{1 - \exp\left(-\frac{h_0 \Gamma}{\tau_1}\right)\right\} \tag{5}$$

where τ_0, h_0, h_1, and $\tau_0 + \tau_1$ stand for the initial critical resolved shear stress, initial hardening rate, asymptotic hardening rate, and back-extrapolated critical resolved shear stress, respectively. Besides, $\Gamma = \int \sum_\alpha |\dot{\gamma}^\alpha| \, dt$ refers to the accumulated shear strain. In addition, the effect of the neighbor grain's deformation system, β, on the current grain's deformation system, α, is also considered by introducing the latent-hardening parameter, $h^{\alpha\beta}$, which is expressed below:

$$\dot{\tau}_c^\alpha = \frac{d\hat{\tau}_{cr}}{d\Gamma} \sum_\beta h^{\alpha\beta} \dot{\gamma}^\beta \tag{6}$$

where $\dot{\gamma}^\beta$ represents the shear rate of β, and $\dot{\tau}_c^\alpha$ is the rate of the critical resolved shear stress (CRSS). Thus, the shear-strain evolution in the deformation system, α, of a specific individual grain can be written as:

$$\dot{\gamma}^\alpha = \dot{\gamma}_0 \left| \frac{\tau^\alpha - \tau_b^\alpha}{\tau_c^\alpha} \right|^{\frac{1}{m}} sgn(\tau^\alpha - \tau_b^\alpha) \tag{7}$$

where $\dot{\gamma}_0$, τ^α, and m denote the reference value of the shear rate, resolved shear stress (RSS), and rate-sensitive exponent, respectively. By solving the microscopic deformation behavior of an individual grain and its interaction with the overall equivalent aggregate composed of all grains, the macro and micro mechanical response of the material can be simulated separately and make connections between the finite plastic deformation modes with macroscope mechanical properties. What's more, the evolution of the back stress in a specific deformation system, α, is also involved in our model for the purpose to explain the Bauschinger effect in cycle loading:

$$\dot{\tau}_b^\alpha = \xi^\alpha sgn(\dot{\gamma}^\alpha) \sum_\beta q^{\alpha\beta} |\dot{\gamma}^\beta| - \eta^\alpha \tau_b^\alpha \sum_\beta q^{\alpha\beta} |\dot{\gamma}^\beta| \quad (8)$$

where the first term is the linear kinematic hardening, and the second term is the dynamic recovery. ξ and η are the corresponding coefficients of the two terms.

2.3 Results

2.3.1 Microstructure of Undeformed Al0.3 HEAs by SEM Analysis

The microstructures of the Al0.3 HEA samples are shown in Figures 2(a) and 2(b). As shown in Figure 2(a), the Al0.3 HEA with a single FCC phase has a homogeneous microstructure. The microstructure of the Al0.3 HEA with an FCC matrix and B2 precipitates are shown in Figure 2(b). The needle-like B2 precipitates with the length less than 2 μm are uniformly distributed in the FCC matrix.

2.3.2 Low Cycle Behavior of the Al0.3 HEAs

The initial tension part and hysteresis loops (stress vs. strain) of the Al0.3 HEA samples under LCF with the strain amplitude of $\pm 1\%$ are shown in Figure 3. In Figures 3(a)(b), the hysteresis loops of the 1st cycle are symmetric in the Al0.3 HEAs with and without B2 precipitate. The yield strength of the FCC Al0.3 HEA is ~ 170 MPa, and the maximum stress at the strain of 1% is ~ 210 MPa, as presented in Figure 3(a). The yield strength and maximum stress of the FCC + B2 Al0.3 HEA are ~ 350 MPa and 420 MPa, respectively, given in Figure 3(b). The initial tension part of the Al0.3 HEA with the B2 precipitate shows work hardening while that of the Al0.3 with a single FCC phase has relatively low hardening behavior. An obvious increase of the maximum stress can be observed in the cyclic tensile stage, compared with the initial tension in both alloys. This trend indicates that the cyclic hardening occurred during the LCF of the Al0.3 at the strain amplitude of $\pm 1\%$. It is worth mentioning that there are unexpected serrated flows on the plastic region of all the hysteresis loops, although the serrated flow usually occurred under the condition of high or cryogenic temperature and low strain rate (~ 10^{-3} or $10^{-4}\ s^{-1}$) [34-41]. The hysteresis loops of different cycles are shown in Figures 3(a) and (b) for the Al0.3 HEA with an FCC phase and FCC + B2 phases, respectively. The increasing maximum stress of the single FCC sample until the 100th cycle indicates an obvious cyclic hardening during LCF. After the 100th cycle, the maximum stresses tend to stay at the same level. On the other hand, the hysteresis loops of the FCC + B2 sample show a very similar shape without obvious cyclic hardening.

The comparison of the relationship of the total strain amplitude versus the reversals to failure ($2N_f$) for different alloys is shown in Figure 4(a), including the present Al0.3 HEA, other representative HEAs and some conventional alloys [18, 25, 42-45]. The Al0.3 HEA with a single FCC phase tends to have higher LCF life, compared to the other alloys at high strain amplitudes (⩾1%). Figure 4(b) shows the relationship of the total strain amplitude as a function of the reversals to failure ($2N_f$). The Al0.3 HEA with a single FCC phase has greater LCF life than the Al0.3 HEA with B2 precipitates at each strain amplitude. The Basquin and Coffin-Manson laws are combined for predicting the LCF life because it contains both the elastic and plastic regions. The Basquin law described as:

$$\frac{\Delta\sigma}{2} = {\sigma'}_f (2N_f)^b \tag{9}$$

where $\Delta\sigma$ is the total stress amplitude; ${\sigma'}_f$ is the fatigue-strength coefficient; N_f is the number of cycles to failure; b is the fatigue-strength exponent. The Coffin-Manson law is given by the following equation:

$$\frac{\Delta\varepsilon_p}{2} = {\varepsilon'}_f (2N_f)^c \tag{10}$$

where $\frac{\Delta\varepsilon_p}{2}$ is the plastic-strain amplitude; N_f is the number of cycles to failure; ${\varepsilon'}_f$ is the fatigue-strain coefficient; and c is the fatigue-ductility exponent. Based on the two equations above, the total fatigue-life prediction can be expressed as:

$$\frac{\Delta\varepsilon}{2} = \frac{\Delta\varepsilon_e}{2} + \frac{\Delta\varepsilon_p}{2} = \frac{{\sigma'}_f}{E}(2N_f)^b + {\varepsilon'}_f (2N_f)^c \tag{11}$$

where $\frac{\Delta\varepsilon}{2}$ is the total strain amplitude; $\frac{\Delta\varepsilon_e}{2}$ is the elastic-strain amplitude; $\frac{\Delta\varepsilon_p}{2}$ is the plastic-strain amplitude; ${\sigma'}_f$ is the fatigue-strength coefficient; E is the elastic modulus; N_f is the number of cycles to failure; b is the fatigue-strength exponent; ${\varepsilon'}_f$ is the fatigue-strain coefficient; and c is the fatigue-ductility exponent. The FCC+B2 Al0.3 HEA shows two modes of deformation in plastic-strain part which are similar with those in the Al0.5

HEA [18]. There could be different plastic deformation mechanisms at high strain amplitudes (1.5% - 1%) and low strain amplitudes (0.75% - 0.25%) in the FCC+B2 Al0.3 HEA

2.3.3 Low Cycle Fatigue Behavior by in situ Neutron Diffraction

The lattice-strain evolutions of different grain families of the Al0.3 HEAs along the loading direction during LCF are shown in Figure 5. The lattice-strain evolutions are related to specific deformation mechanisms [46, 47]. The lattice-strain evolutions of the {200}, {220}, and {331} grain families of the FCC Al0.3 along the loading direction during initial tension are exhibited in Figure 5(a). The lattice strains in the initial tension of the FCC Al0.3 increase linearly with the applied stress. The first vertical inflection of the lattice strain could be observed at ~ 123 MPa in {311} and {220} grain orientations, while the inflection in {200} is horizontal. This feature indicates that the {200} grain family along the loading direction tends to share more load during the tensile deformation. The third vertical inflection is at the stress of ~ 158 MPa in the {200} grain family. This trend suggests the macro yielding of this alloy is strongly associated with the inflection point of the {200} grain family. Figure 5(b) presents the lattice-strain evolutions of {200}, {220}, and {311} grain families of the FCC phase and {110},{200}, and {211} grains of the B2 phase in the FCC + B2 Al0.3 HEA during initial tension. The lattice strains of grain families of FCC {200} and FCC {311} turn upward firstly at ~ 350 MPa while others have horizontal inflections. The FCC {220} has its first upward trend at ~ 370 MPa. The macro yielding of Al0.3 HEA with B2 precipitates is associated with the yielding point of the FCC {200} which is also observed in the single FCC Al0.3 HEA. The grain families of B2 phase tend to share more load for their horizontal trends, especially the B2 {200} grain orientation.

In Figures 5(c)(d), the lattice-strain evolutions of different grain families of the Al0.3 HEAs along the loading direction during the 1^{st} LCF cycle are plotted. The lattice strain hysteresis loops are symmetric in the two alloys. The lattice-strain evolutions in the reverse compression and following tension parts are similar to the initial tension. In the Al0.3 with a single FCC phase, shown in Figure 5(c), the FCC {220} grain family has almost no lattice-strain hysteresis loop compared to the FCC {200}. For the Al0.3 with B2 precipitates, instead of FCC {220}, the FCC {200} grain family has no obvious lattice-strain loop while B2 {200} takes the largest loop, as presented in Figure 5(d). As a result of the strain partitioning in FCC+B2 Al0.3, the grain families of hard B2 phase behave clockwise (or towards the right), and those of the soft FCC matrix go anticlockwise (or going upward).

2.3.4 Microstructures of Deformed Al0.3 HEAs after LCF

The fracture surface of the failed Al0.3 with single FCC phase after LCF with the strain amplitude of $\pm 1\%$ is shown in Figures 6(a) and 6(b). As shown in Figure 6(a), the crack initiated at the surface and propagated into the sample. In Figure 6(b), the striations near the crack-initiation site show a stable crack-growth region, which indicates the transgranular ductile fracture feature. There are secondary cracks accompanying with the striations near the crack initiation, which could influence the crack-propagation process in a certain extent.

The dislocation structures of the fractured Al0.3 with a single FCC phase after LCF are shown in Figure 7. A high density of interacting dislocations can be observed, which form the dislocation tangles. The main deformation mechanism in the Al0.3 with an FCC phase is dislocation slip. No twinning is found in the failed Al0.3 after LCF with the strain amplitude of $\pm 1\%$.

2.4 Discussions

According to the TEM results, the initial strain hardening of the Al0.3 under LCF with the strain amplitude of $\pm 1\%$ could be attributed to the dislocation generation and interactions. The evolution of the dislocation density is investigated, using the relationship between dislocation density of a certain lattice plane and its FWHM of the diffraction peak. Since the dislocation density has a proportional relationship with the FWHM, we can use the evolution of FWHM to illustrate the evolution of dislocation density. Figure 8(a) shows the FWHM evolution of the FCC {200} and {220} in the FCC Al0.3 HEA from the initial tension to the 2nd cycle with a strain amplitude of 1%. All the FWHM values of the grain families showed an increasing trend during the initial tension to the strain of 1%. Then in the reverse compression part, the FWHM decreased to a valley point at the strain of ~ 0%, i.e., a load-free condition, and increased again as the strain reaching -1%. Similar decreasing-valley-increasing of FWHM can be observed in the following tensile and compressive stages. The FWHM values at the strain ~ 0%, i.e., a load-free condition, could be used to illustrate the accumulation of dislocations because there is the minimum influence of the applied load at this point. The FCC {200} peak has obvious broadening at the load-free points, compared with the initial point, while the FCC {220} peak has relatively small broadening in the Al0.3 with a single FCC phase. This trend indicates that the FCC {200} grain family has higher accumulation of dislocations than FCC {220}. The FWHM vs. applied engineering strain of the FCC {200}, FCC {220}, and B2 {110} in the FCC + B2 Al0.3 HEA is exhibited in Figure 8(b). The B2 {110} peak of the B2 phase has the largest broadening at the load-free points. The accumulation of dislocations is higher in the B2 phase than in the FCC matrix. As shown in Figure 5(c), in the Al0.3 with a single FCC phase, the FCC {200} grain family has larger hysteresis loops than the FCC {220} due to the higher accumulation of dislocation in FCC {200}. For the Al0.3 with B2 precipitates, the hysteresis loops of the B2 phase are larger than those of the FCC phase due to the higher dislocation accumulation in the B2 phase.

The EVPSC model is firstly calibrated with the uniaxial tension experiment results. The applied modeling of the FCC Al0.3 HEA adopted a random texture. In Al0.3 HEA, the dominant plastic-deformation mode is the $\{1\bar{1}1\}\langle 110\rangle$ dislocation-slip system, which is very common in the FCC structure of Al_xCoCrFeNi when the Al content is less than 7% [18]. In addition, we also extract the cyclic-mechanical response of this alloy. Figure 9(a) illustrates the comparison between the mentioned two methods for specific cycles, where the initial tension and first 10 cycles of simulated results are compared to the specific experiment data, i.e., initial tension, 1st, 2nd, 5th and 10th cycles. Simulation results show good agreement with the experiment data. The plastic-deformation and work-hardening behaviors are mainly related to the $\{1\bar{1}1\}\langle 110\rangle$ glide and its hardening parameters used in the Voce hardening laws mentioned in Eqs. (4) and (7) are listed in Table 1. It can be seen that with the increase of the number of cycles, the simulation results reveal the trend of the increasing stress amplitude. This result is consistent with the trend of the experiment and shows the cyclic-hardening effect of this alloy in the low-cycle number range. However, a similar phenomenon was observed in $Al_{0.5}CoCrFeNi$ under cyclic loading within the initial cycles[18], where rapid multiplication of dislocations existed. Another phenomenon should be noted is that the premature yielding behavior happens during the subsequent cycles after the initial tension. This result mainly correlates to the so called Bauschinger effect, which results from the kinematic-hardening mechanism and is common in some magnesium alloys [47]. The existence of this effect causes a gentle rather than sharp change at the excessive position from relaxation to reverse loading. Nevertheless, cyclic-loading curves of $Al_{0.3}CoCrFeNi$ show strong tensile-compressive symmetry, where the stress level at the left lower corner is in the same range of that at the right upper corner.

In order to further reveal the microscopic-deformation behavior of the Al0.3 with a single FCC phase under cyclic loading, the lattice-strain evolutions are simulated. Figure 10 illustrates the lattice strain versus applied uniaxial stress of $\{200\}$, $\{220\}$ and $\{311\}$ grain families within the initial tension, 1st cycle compression and tension, 2nd cycle compression and tension, and 5th cycle compression along the loading direction, respectively. For the initial tension in Figure 10(a), the lattice strain will firstly change linearly under ~ 123 MPa, where the material is under elastic deformation. However,

$\{220\}$-oriented grains show larger directional stiffness, as compared to the other two sets of grains. When the applied stress exceeds 123 MPa, the lattice strain will undergo obvious deflection, especially the $\{200\}$- and $\{220\}$-oriented grains, which indicates that the material has begun to undergo plastic deformation, and at the same time, the redistribution of the stress occurs between the grains of different orientations. Since the $\{220\}$-grain family is softer, the deformation that can be accommodated within these grains is reduced, causing the lattice strain to deflect to the left. On the other hand, the $\{200\}$ grain family can accommodate more deformation with increasing their lattice distortion. During the 1st compression in Figure 10(b), the lattice-strain evolution of the three specific crystal planes has the same discipline as the initial stretching stage, that is, the $\{220\}$ yields first, and the $\{200\}$ can accommodate more deformation under the same stress level. It is worth noting that the simulated results show that there is a certain residual strain in the three orientation grains at a zero-stress level. Among them, the $\{200\}$ has larger a positive ~ 0.053% residual lattice strain, which is caused by the accommodation of more deformations during the forward loading process but not the complete release during the reverse loading process. As for $\{220\}$ and $\{311\}$ grain families, they can accommodate with less deformation, and the yielding occurs earlier with smaller accumulated lattice strains, which are almost completely released during the reverse loading process, resulting in relative smaller residual lattice strains that are close to 0. Nevertheless, similar evolution exists within the following cycles, which can be observed in Figures 10(c-f). It can be found that the redistribution of stress seems to be more inclined between the $\{220\}$ and $\{200\}$, while the lattice strain of the $\{311\}$-oriented grains hardly undergo obvious deflection. Thus, it is foreseeable that during the entire cyclic-loading process, there is a stable and periodic stress redistribution and strain-release process between grains of different orientations in the Al0.3 with a single FCC phase.

Back stresses are usually used to understand the dislocation behavior of metals and alloys under cyclic loading [48]. Dislocations will pile up against the interfaces to increase the plastic heterogeneity between different phases, which may lead to an increase in the back stress with the increasing cyclic numbers in low strain amplitudes [28]. The back stresses resulted from the dislocation accumulation of the incoherent precipitate could cause a lower LCF life. As shown in Eq. (8), the evolution of the back stress in a specific micro deformation system α mainly contains two terms (ξ and η) in the simulation. The ξ represents the linear kinematic hardening and the η is for the dynamic recovery. As can be seen in Table 1, the value of ξ increases dramatically from 3000 in the FCC sample to more than 11000 in the FCC+B2 sample, while the η values are similar in the two samples The effect of linear kinematic hardening term related to the coefficient ξ on back stress is dominant. This means that the introduction of the B2 precipitates mainly affects the kinematic hardening of α system in the matrix grains, while the effect on dynamic recovery is relatively weak. From the simulation results, the value of ξ does increase due to the appearance of B2 phase, indicating that the B2 precipitate and its accompanying plastic heterogeneity indeed increase the overall back stress of the material. Therefore, the introduction of the B2 phase mainly increases the total back stress by affecting the kinematic hardening effect of the matrix grain slip system, and the increase in the back stress could be one of the main reasons for the decrease in the fatigue life of $Al_{0.3}CoCrFeNi$ with B2 precipitates.

Besides the back stress, the effect of PSBs could be another way to explain the LCF life. The PSBs play an important role in the fatigue-crack initiations at fatigue slip bands, grain and twin boundaries inclusions, pores and other inhomogeneities [49-52]. As can be seen in the Figures 5(a) and 5(b), the data of FCC grain families have more obvious vertical trends after yielding in the FCC + B2 alloy than those in the single FCC alloy due to the highly increased tensile strength by B2-precipitate strengthening. With the enhancing strengths by the hard B2 phase, the “soft” or easy deforming FCC grain families need to take more plastic shear strains, which could be resulting into the formation of PSBs [53, 54]. The improvement on the generation of PSBs provide more fatigue-crack-initiation sites, which could lead to the shorter fatigue life. On the other hand, the incoherent B2 precipitate could hinder the movement of the dislocations carried by PSBs and make them much harder to travel intergranularly and transgranularly in the FCC + B2 HEA than in the single FCC HEA. The dislocations within PSBs will pile-up and accumulate faster in the precipitate strengthened HEA which could lead to the early crack initiation and then fatigue failure of the samples.

2.5 Conclusions

The B2 precipitates could increase the yield strength and decrease the LCF life in the $Al_{0.3}CoCrFeNi$ HEA. During cyclic loading, the grain families of hard B2 phase tend to go clockwise (or towards the right) while those of the soft FCC matrix behave anticlockwise (or going upward). The low cycle fatigue behavior the $Al_{0.3}CoCrFeNi$ HEA could be simulated nicely from the in situ neutron diffraction measurements with the EVPSC model. The simulation results indicate that the B2 precipitates could increase the back stresses during cyclic loading by facilitating the kinematic hardening in the matrix, while the effect of dynamic recovery is relatively weak. On the other hand, the "soft" FCC grain families need to take more plastic shear strains due to the highly increased tensile strength by the "hard" B2 precipitate, which could promote the formation of PSBs in the FCC matrix. The lower LCF life of the $Al_{0.3}CoCrFeNi$ HEA with B2 precipitates could be caused by the increase of back stress and promotion on the formation of PSBs, which could provide more crack-initiation sites leading to a shorter fatigue life.

APPENDIX

Table 1. Hardening parameters used in the EVPSC model. Parameters related to the back stress are included in the brackets only for the cyclic-loading condition.

Sample	Phase	Hardening parameters (MPa)				Back Stress (MPa)	
		τ_0	τ_1	h_0	h_1	ξ	η
Al0.3-FCC	FCC	62	20	40	0	3,000	110
Al0.3-FCC+B2	FCC	71	57	62	44	⩾11,000	127
	B2	321	26	47	33		

Table 2. Fitting parameters for the Basquin and Coffin-Manson laws.

	σ'_f(MPa)	ε'_f	b	c	E (GPa)
FCC	**194.5416**	**0.684258**	**-0.008**	**-0.555**	**157.2**
FCC+B2	**3343.364**	**8.576893**	**-0.188**	**-1.004**	**180.1**

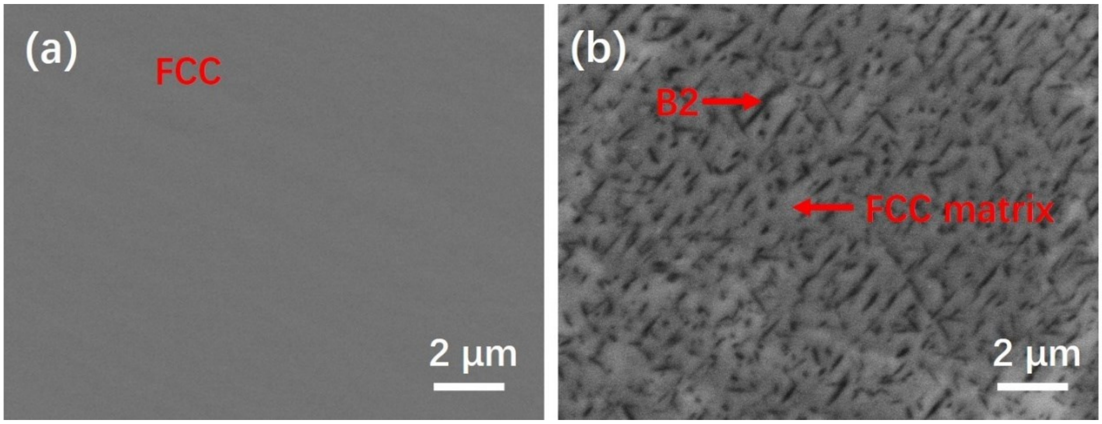

Figure 2. The microstructures of the $Al_{0.3}CoCrFeNi$ HEA (a) with a single FCC phase and (b) with FCC + B2 phases by SEM.

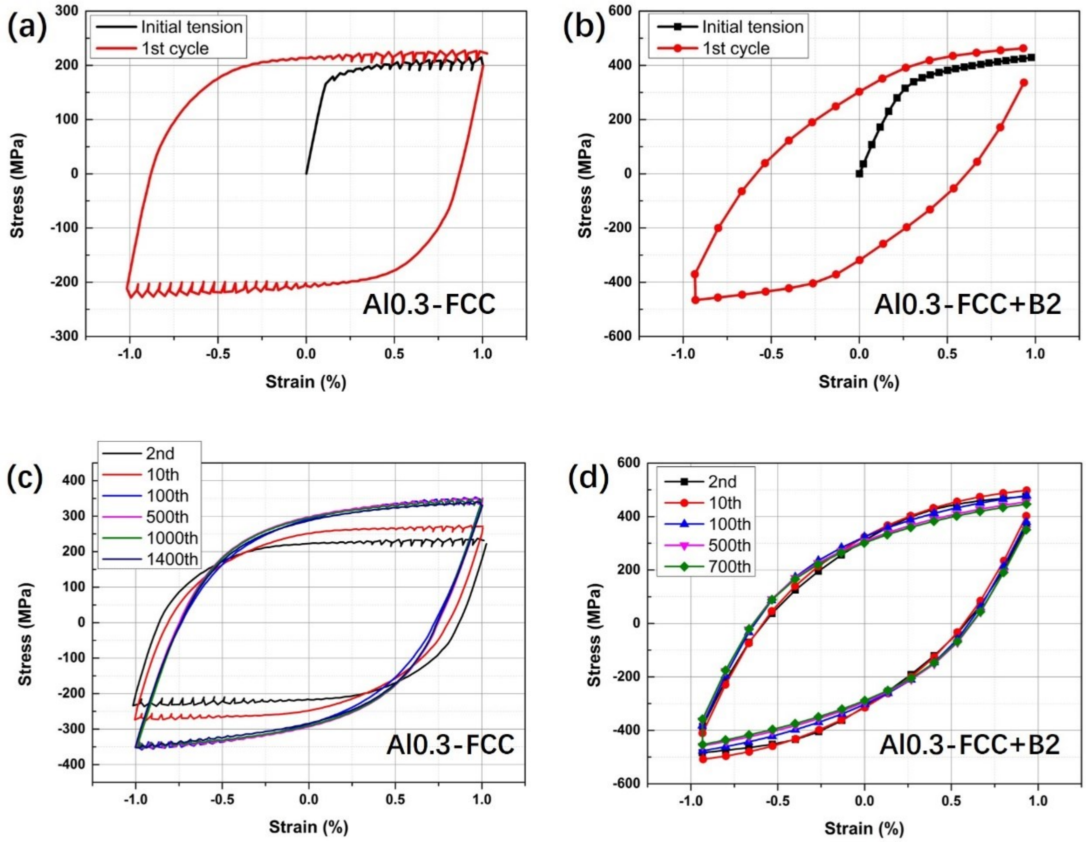

Figure 3. The initial tension and hysteresis loops of the $Al_{0.3}CoCrFeNi$ HEA (a)(c) with a single FCC phase and (b)(d) with FCC+B2 phases at the strain amplitude of 1%.

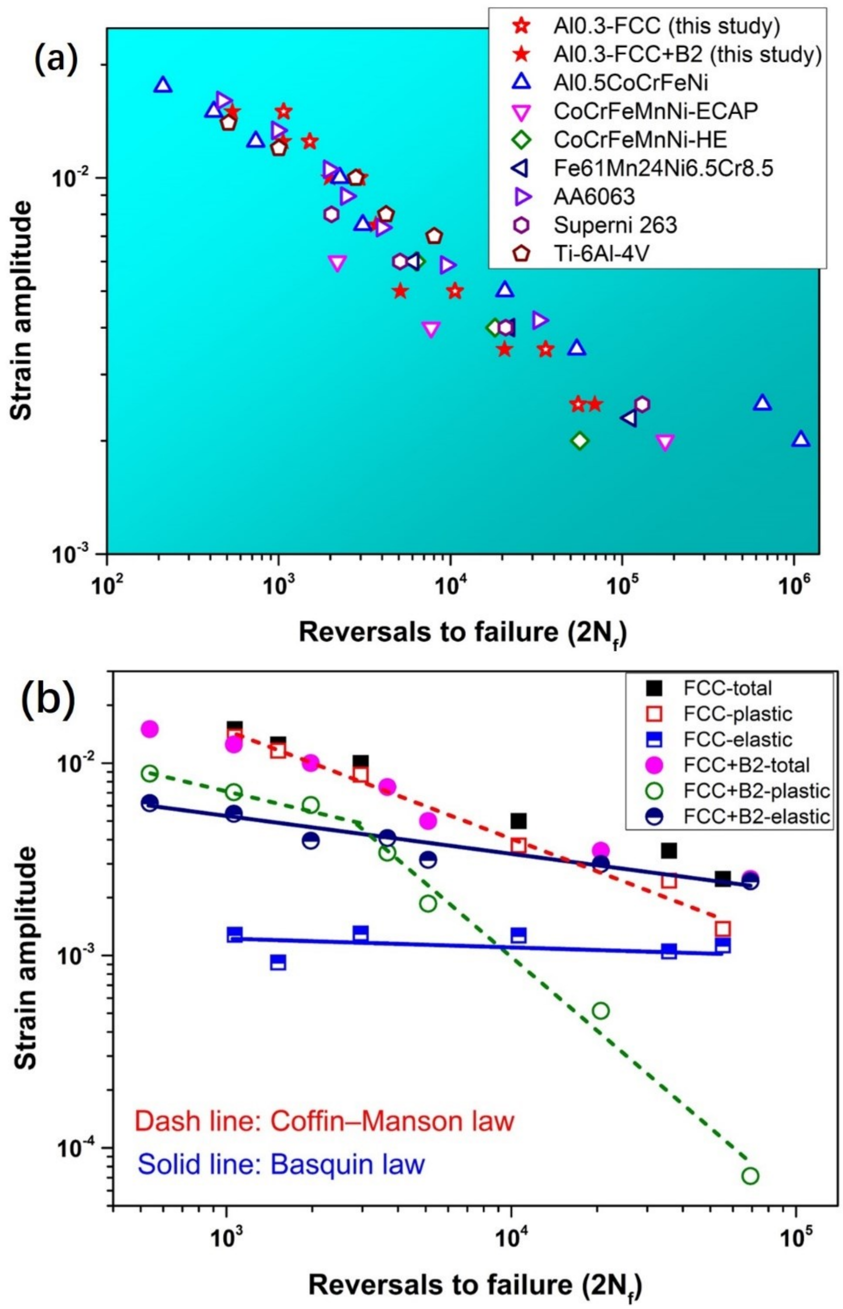

Figure 4. (a) The comparison of low cycle fatigue data for the present alloys, other HEAs, and conventional alloys [18, 25, 42-45]. (b) The total strain amplitude, plastic strain amplitude, and elastic strain amplitude vs. the number of reversals to failure for the $Al_{0.3}CoCrFeNi$ HEA HEAs with a single FCC phase and with FCC + B2 phases, which are used for Coffin-Manson & Basquin analyses.

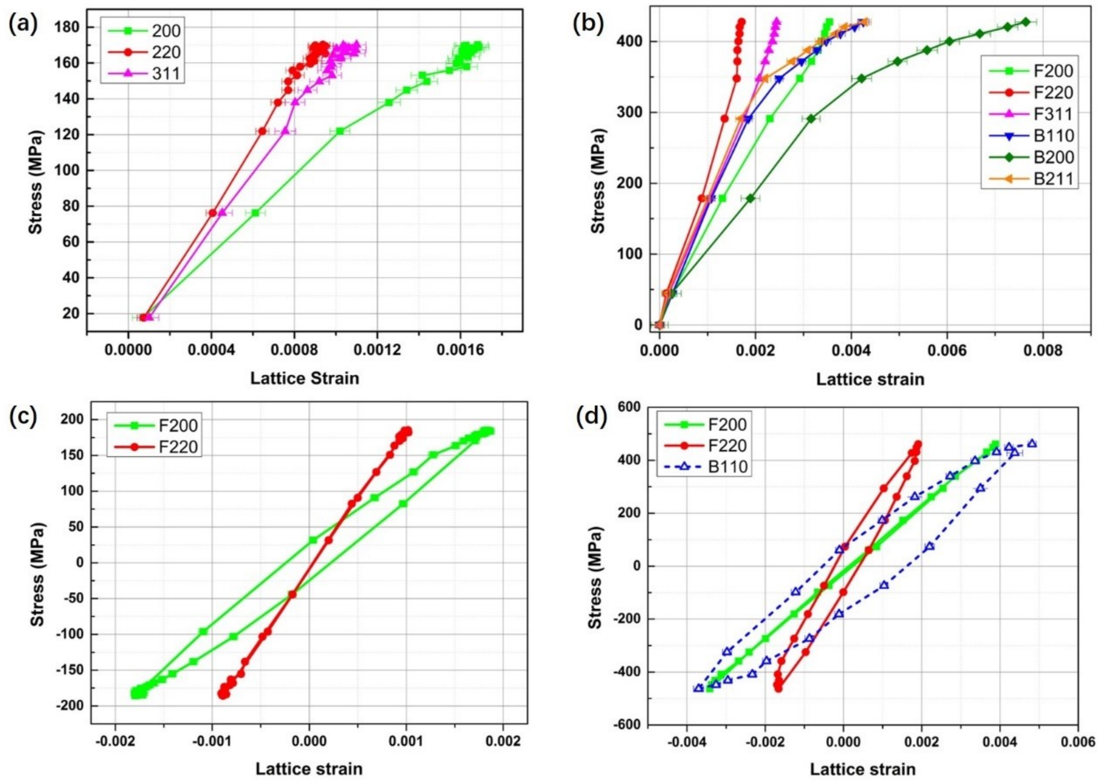

Figure 5. The lattice-strain evolutions along the loading direction of the $Al_{0.3}CoCrFeNi$ HEA (a)(c) with a single FCC phase and (b)(d) with FCC + B2 phases at the strain amplitude of 1%. (a)(b) are initial tension part and (c)(d) are the 1st cycle.

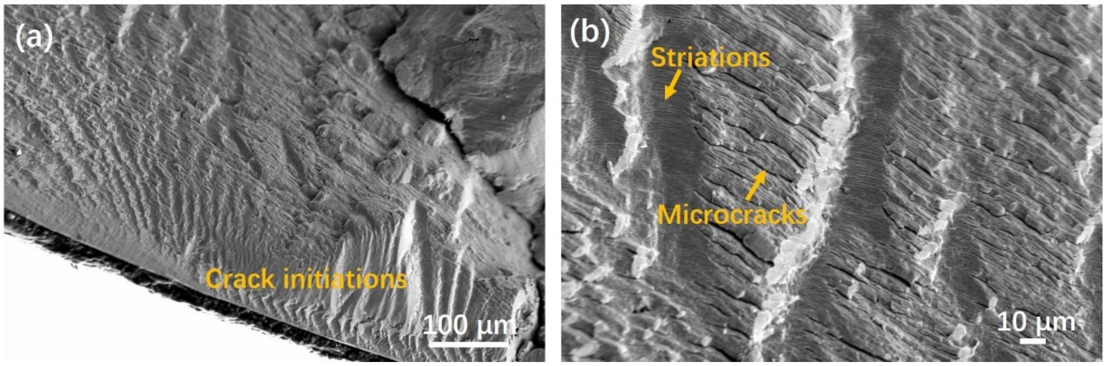

Figure 6. The SEM results of the fracture surfaces of the FCC $Al_{0.3}CoCrFeNi$ HEA after LCF (a) crack initiation; (b) striations and secondary cracks near the crack-initiation site.

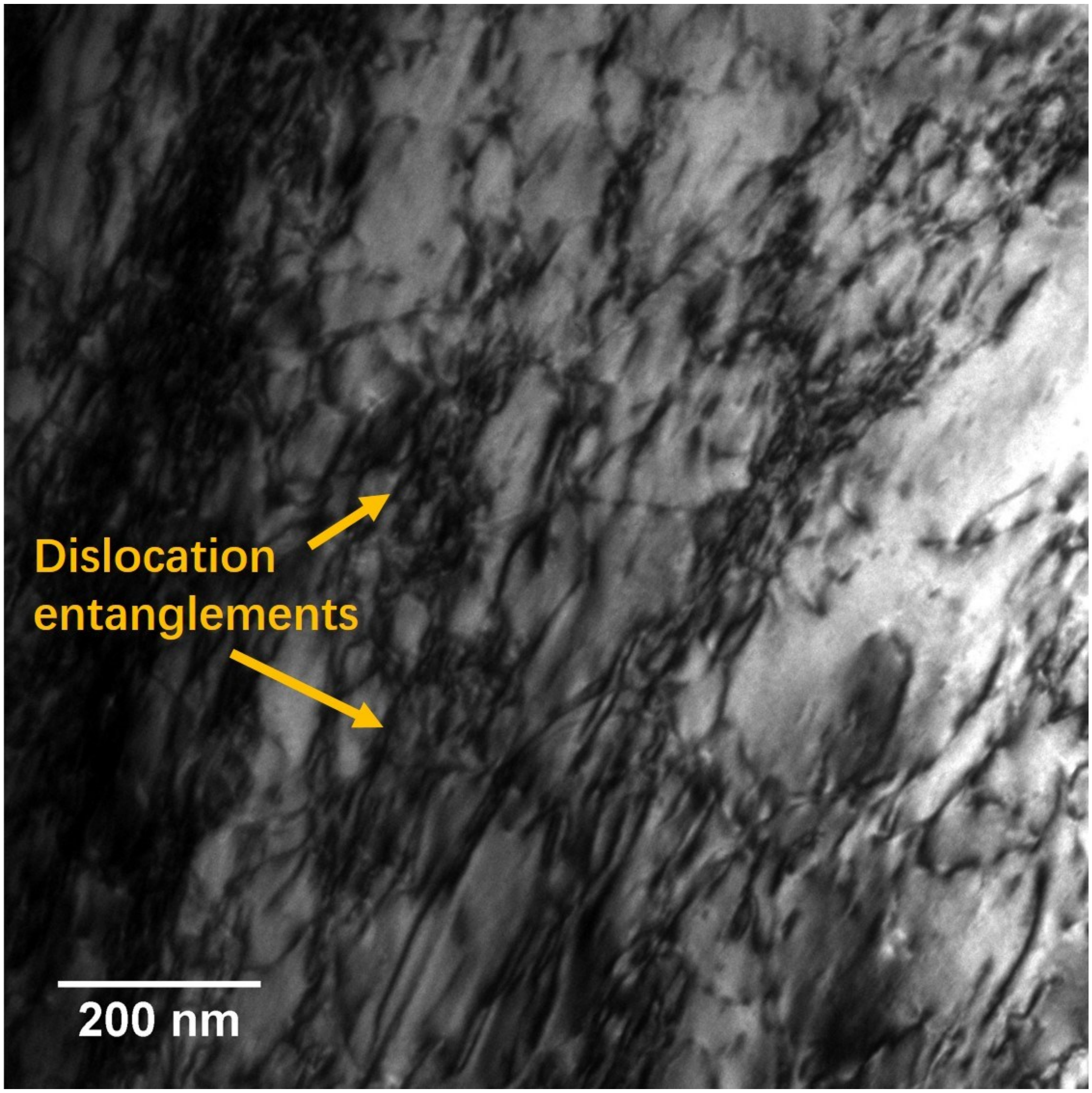

Figure 7. The TEM image of dislocation structures in the $Al_{0.3}CoCrFeNi$ HEA with a single FCC phase after LCF.

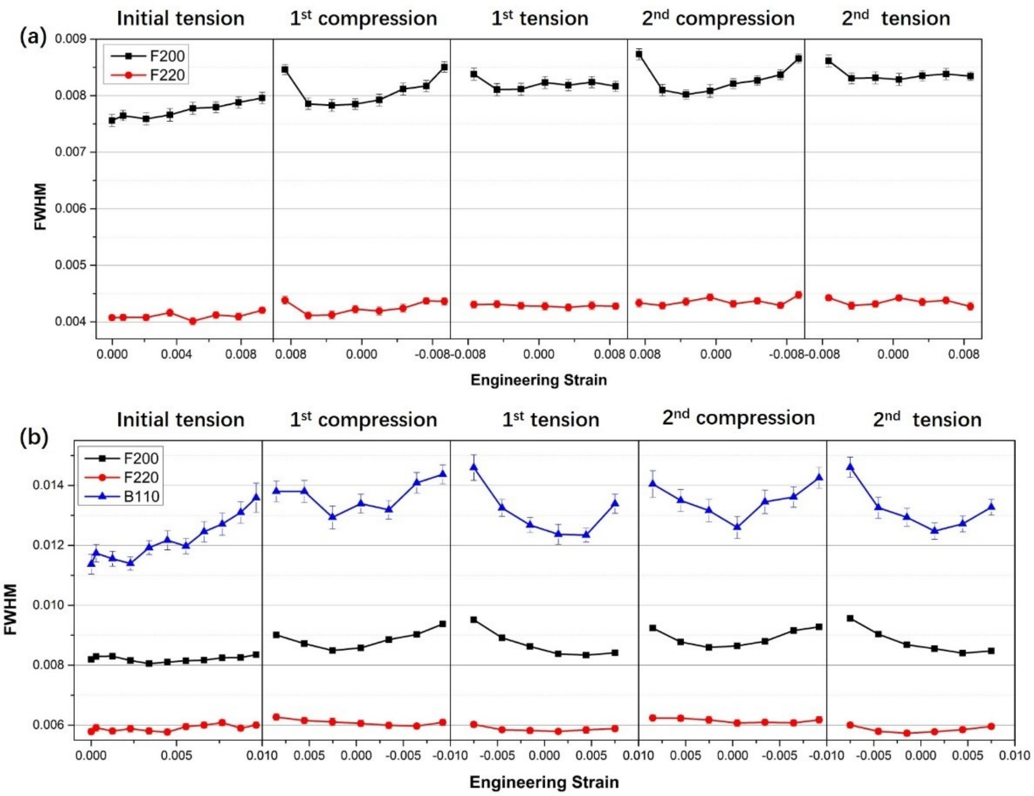

Figure 8. The FWHM vs. applied engineering strain of the $Al_{0.3}CoCrFeNi$ HEA (a) with a single FCC phase and (b) with FCC + B2 phases at the strain amplitude of 1%.

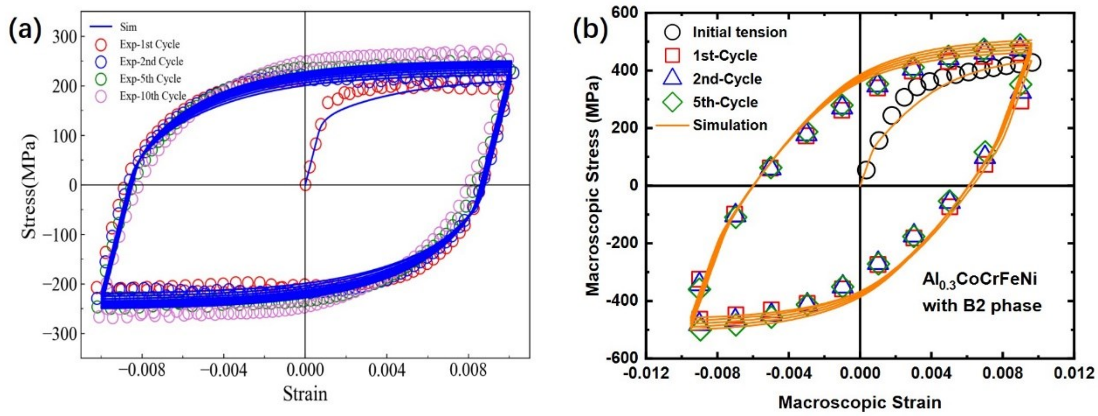

Figure 9. (a) True stress-strain curves and (b) cyclic response of the initial tension and the first 10 cycles of experiment with the corresponding EVPSC simulation results of the FCC $Al_{0.3}CoCrFeNi$ HEA.

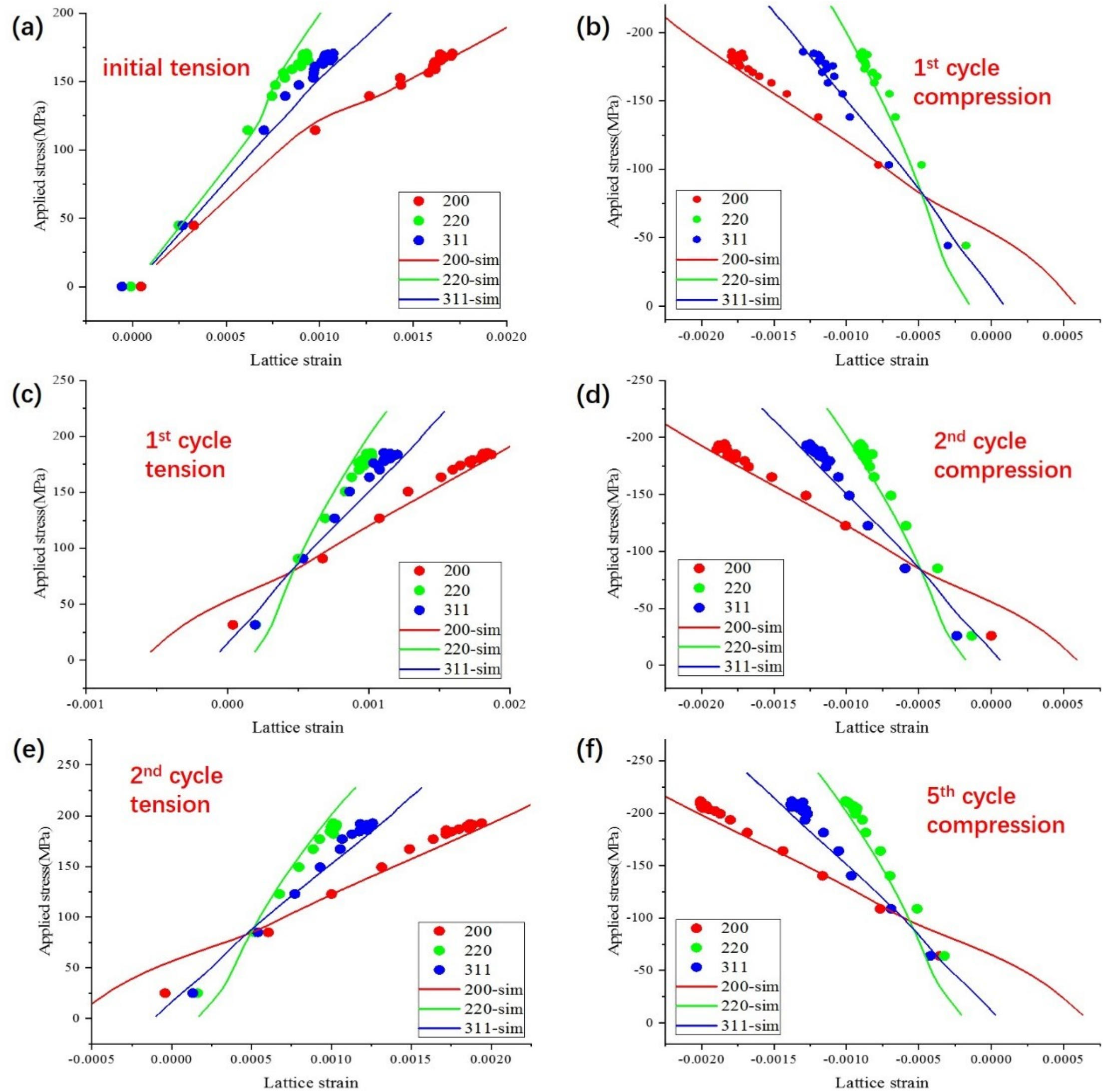

Figure 10. Lattice-strain evolution with applied stress for specific grain families of the FCC $Al_{0.3}CoCrFeNi$ HEA during (a) initial tension, (b) 1st cycle compression, (c) 1st cycle tension, (d) 2nd cycle compression, (e) 2nd cycle tension, and (f) 5th cycle compression.

CHAPTER 3.
IN SITU NEUTRON DIFFRACTION INVESTIGATION ON THE DEFORMATION BEHAVIOR OF INTERSTITIAL METASTABLE HIGH ENTROPY ALLOYS

Abstract

Different annealing processes on the interstitial metastable HEAs provided a series of tensile properties that exceed most of the conventional alloys and steels. The underlying mechanisms were investigated via real-time in situ neutron diffraction. The FCC-to-HCP transformation was revealed to play a critical role in the multistage work hardening behavior that leads to the strength-ductility tradeoff. The activation of transformation could be tuned by different annealing processes, which triggers the subsequent load sharing and redistribution between FCC and HCP phases. By facilitating the FCC to HCP transformation, more loads are shared by the HCP-martensite and the FCC phase can take more plastic deformation, which could increase the strength and ductility of the HEAs. This work could help to further design the HEAs to overcome the strength-ductility tradeoff and will be beneficial to the engineering applications.

3.1 Introduction

Metals and alloys, which are widely used as structural materials, have been extensively studied on their mechanical properties. Nowadays, with the demand of high-performance materials for industrial applications, more and more efforts have been devoted to seeking alloys with both high strength and ductility. However, the strength-ductility trade-off exits in most of metals and alloys, which means that increasing strength will lead to a sacrifice of ductility. High entropy alloys (HEAs), as a new alloying strategy in the past decade, opened an extremely wide space of compositional design and have been proved to have desirable mechanical properties [1-3, 9-11, 22, 23, 55-57]. Several different pathways have been investigated in HEAs to break the strength-ductility trade-off, such as precipitations [57], gradient structures [22], hierarchical microstructures [23, 58], phase transformations [9, 58, 59], interstitial solid solution [58, 59], interstitial complexes [10]. An interstitial carbon doped HEA with a hierarchical microstructure [58, 59] has been developed recently which presents an efficient way to improve strength and ductility simultaneously by triggering transformation induced plasticity (TRIP) and twinning induced plasticity (TWIP) effects. The ductility could be improved from 14% to 60% by a multi-stage work hardening behavior which is related to the sequential activation of TRIP and TWIP effects resulting from the large variation in phase stability facilitated by hierarchical grains [58]. An excellent tensile performance, i.e., 1.05GPa of ultimate tensile strength and 35% of elongation, was achieved due to improved work hardening caused by face-centered cubic (FCC) to hexagonal closed-packed (HCP) martensitic transformation in confined regions and twinning [59]. The deformation mechanisms of the interstitial HEA with hierarchical microstructures were discretely studied by electron backscatter diffraction (EBSD), transmission electron microscopy (TEM), and digital image correlation (DIC). However, the panorama of continuous deformation mechanism evolutions of the carbon doped under loading is still not revealed because of the limitations of the post-test techniques and surface measurements. Both the post-mortem and surface measurements cannot quantitatively identify the load partitioning of different phases as well as grain orientations and hardly have the ability of tracking activations and changes of deformation mechanisms. In this way, there are still blank spaces left in the understanding of consequences of dislocations, twins, new phases and their interactions on the deformation behaviors of the metastable HEAs, such as the work hardening behavior.

In this work, a wide range of strength-ductility was achieved in the interstitial metastable HEAs by different treatments, which has an obvious improvement compared with the conventional alloys and steels. The real-time in situ neutron diffraction was used to investigate the whole picture of deformation mechanism evolutions of the interstitial metastable HEAs under uniaxial tension, especially for the FCC to HCP martensitic transformation. Diffraction patterns during the whole process of tensile test could be acquired continuously, which provide bulk average information over a certain gauge volume. The activations and evolutions of TRIP, as well as other deformation mechanisms at the lattice level, were determined, which correlate to the work hardening behavior. The samples with high-strength-low-ductility, medium-strength-ductility, and low-strength-high-ductility were proved to have different styles in deformation behavior for different grain orientations via the lattice strain evolutions. This work could fill the blank of the deformation mechanisms and enrich the knowledge of strength-ductility tradeoff systematically in interstitial TRIP HEAs with hierarchical microstructures by the conventional post-test/surface measurements and further promote the engineering applications of HEAs.

3.2 Experimental

The studied metastable $Fe_{49.5}Mn_{30}Co_{10}Cr_{10}C_{0.5}$ alloy (at.%) [58] was prepared with pure elements (>99.9% wt.%) by vacuum induction melting and casting. Then the alloy was hot rolled at 900 °C with a reduction of 50% in thickness. After hot-rolling, the alloy was homogenized at 1200 °C for 2 h followed by water-quenching. Finally, cold rolling was conducted with a thickness reduction of 50%. Then the plate dog-bone samples were cut with the dimensions of 3*2.6*15 mm in gauge section. Three different heat treatment were used to create a series of different microstructures, i.e. 650 °C for 15 min, 700 °C for 6 min, and 750 °C for 30 s, 1 min, 2 min, 3 min followed by water-quenching and corresponding samples denoted as P650C-15m, P700C-6m, P750C-30s, P750C-1m, P750C-2m, and P750C-3m, respectively. On the other hand, rod dog-bone samples were cut with the dimensions of Φ 8*16 mm in gauge section. Three different heat treatment were conducted on the rod dog-bone samples, i.e. 650 °C for 15 min, 700 °C for 6 min, and 750 °C for 3 min followed by water-quenching and corresponding samples denoted as R650C-15m, R700C-6m, and R750C-3m, respectively. The strain-controlled LCF tests were performed with an MTS Model 810 servo-hydraulic machine at ambient temperature. The strain amplitudes are ±1.25%, ±1.0%, ±0.75%, and ±0.5%, respectively. The strain rate is $1 \times 10^{-2}\ s^{-1}$ and the initial loading is tension.

The in situ neutron-diffraction test under uniaxial tension was performed, using an MTS load frame at the VULCAN Engineering Materials Diffractometer [29, 30], the Spallation Neutron Source (SNS), Oak Ridge National Laboratory (ORNL). The in situ neutron diffraction data were analyzed via the VULCAN Data Reduction and Interactive Visualization software (VDRIVE) [31].

3.3 Results and Discussions

The tensile engineering stress-strain curves of the studied samples subjected to different annealing processes are shown in Figure 11(a). The P750C-3m, P700C-6m, and P650C-15m samples have the yield strengths of ~400 MPa, ~450MPa, and ~500 MPa, respectively. For the rod samples with same heat treatments, the yield strengths of R750C-3m, R700C-6m, and R650C-15m are ~1040 MPa, ~1016 MPa, and ~900 MPa, respectively. The big rod samples showed dramatically higher yield strength than the thin plate samples and the two batches of samples have opposite trends of yield strengths as the change of annealing temperatures. The total elongations of R750C-3m, R700C-6m, and R650C-15m are 11.3%, 15.5%, and 20.3%, respectively, which are all smaller than the corresponding plate samples. It needs to mention that the P750C-3m, P700C-6m, and P650C-15m samples were tested for both loading and unloading behaviors by loading to 30%, 30%, and 25%, respectively, before sample fracture. For the plate samples treated at 750 °C with different times, P750C-30s, P750C-1m, and P750C-2m have the yield strengths of 989 MPa, 794 MPa, and 450 MPa, accompanying with the total elongations of 1.6%, 24.4%, and 46.5%, respectively. The yield strength was increased with the decrease of annealing time. After yielding, all the samples show a continuous hardening with gradually decreasing rate θ, which is calculated by $\theta = d\sigma_{true}/d\varepsilon_{true}$ where σ_{true} is true stress and ε_{true} is true strain, during uniaxial tension as presented in Figure 11(b). The R750C-3m and R700C-6m showed an almost linear reduction of the strain hardening rate until necking and took the area of low hardening rates. The P750C-1m, and P750C-2m possessed the part of medium hardening rates, while P750C-3m, P700C-6m, P650C-15m, and R650C-15m located the zone of high hardening rates as can be seen in Figure 11(b). Multistage work hardening behavior could be observed for most of the samples other than R750C-3m and R700C-6m. The stage I (<1.2%) could be a quick drop of work hardening rate which is usually related to the dislocation rearrangement [60]. In stage II, the work hardening rates continue to decline with a much low slope compared to stage I. The trend of work hardening rate in stage III is similar to that in stage II, whereas stage III has lower slope of hardening rate. However, there is an obvious increase followed by a decrease of hardening rate in the P750C-2m sample during the strain stage of ~12.9% to 15.6%.

The lattice strain evolutions by in situ neutron diffraction under uniaxial tension are presented in Figure 12. The load partitioning among different grain families can be differentiated with the lattice strain evolutions, which indicate the average stress of corresponding grain families along the loading direction. All the grain families of different samples along loading direction deformed elastically with a linear relationship between true stress and lattice strain at the first stage. After the linear part, the lattice strain of {220} grain family had the first obvious upward trend for all the plate sample except for the P750C-30s which had almost no plastic deformation as shown in Figure 12 (b-f). These transition points of {220} grain family are identical with the yield points of the corresponding samples. For the bar samples in Figure 12 (g-i), the first obvious upward turns of lattice strain happened in the {111} grain family, which are consistent with the yield stresses of the samples. It indicates that the {220} and {111} grain families play more important roles on the yielding process than other grain families in the plate samples and bar samples, respectively. The {200} grain family along loading direction tends to share the largest load during deformation than other grain families in all the studied samples. For the P750C-2m, P750C-3m, P700C-6m, and P650C-15m in Figure 12 (c-f), they had low strength and high ductility, as well as high hardening rate, tending to have an early FCC to HCP transformation at the stress of ~800 MPa. As a result of this early HCP martensite formation, the HCP phase started to share load from FCC phase and then the lattice strain of {311} grain family bends up while {200} grain family almost keep its original trend. The samples with medium strength-ductility-hardening rate, i.e., P750C-1m and R650C-15m, tend to have later phase transformation at 1000-1200 MPa as shown in Figure 12 (b) and 12 (i). In this case, the HCP martensite may not change the intergranular strain a lot in the FCC phase. Therefore, the {311} lattice strain kept a linear trend and {200} lattice strain bended to the right indicating more load shared by the {200} grain family. For the samples with higher strength, low ductility and low work hardening rate, such as R750C-3m and R700C-6m, the HCP formed very late at the stress of ~1350 MPa as can be seen in Figure 12 (g) and 12 (h). The HCP martensite did not have the opportunity to share load from the FCC phase before the lattice strain of {311} grain orientation starting to bend to the right.

The normalized intensity evolutions from in situ neutron diffraction along with the true stress are plotted in Figure 13. The samples with ductility around 25%, i.e. P750C-1m (~24.4%), had almost equal level on the change of intensities in longitudinal direction (LD) and transverse direction (TD) for {111}, {200}, and {311} grain families. For the samples with higher ductility (>25%), such as P750C-2m, P750C-3m, P700C-6m, and P650C-15m, the {111} grain family had more change of normalized intensity in LD than TD as the true stress increasing. On the other hand, for R750C-3m, R700C-6m, and R650C-15m, and P650C-15m with ductility less than 25%, the {311} grain family showed more variation of intensity in LD than TD while the {111} grain family had relatively identical change of normalized intensity in both directions. The deformation in {111} grain family could make the more contributions on the ductility than other grain families. It is worth to mention that the {220} grain family for most of the samples had a dramatical decrease of intensity in LD with relatively small intensity change in TD. This indicates that the {111} grain family along loading direction could be closely related to the FCC to HCP phase transformation.

The FCC fraction evolutions of P750C-1m and P750C-2m are shown with the true stress-strain curves in Figure 14. As shown in Figure 14(a), in P750C-1m ,the decrease of FCC phase fraction occurred at the early stage of plastic deformation and there are two slow reducing trends of FCC phase (true strain 3.2%-5.6% and 8.3%-21%) and one fast decreasing part at 5.6%-8.3% of true strain. For the P750C-2m shown in Figure 14(b), two quick decreasing parts of FCC fraction are located in the true strain of 11%-11.7% and 15.5%-17.6% while two stable sections are observed in 11.7%-15.5% and 17.6%-37.7% in true strain. Since FCC to HCP transformation has a close relation with stress [61], the stresses of starting points of FCC fraction decrease in P750C-1m and P750C-2m are ~953 MPa and ~787 MPa, respectively, indicating that the activation of phase transformation is easier in P750C-2m than P750C-1m. This could relate to the variations of stacking fault energy (SFE) [62, 63] and grain size [64] by different annealing processes. The nucleation and growth of HCP phase are mainly accomplished by overlapping of stacking faults controlled by the movement of Shockley partial dislocations [65]. The decrease of FCC fraction was suppressed after the true strain reached to ~20%, which could be related to higher activation stresses to nucleate the transformation in the ultrafine recrystallized grains [65-67] and the impeding effect of high dislocation density at large strains [65, 68]. The special increasing stage (12.8%-15.6% in true strain) of the work hardening rate could be attributed to the nucleation of HCP-martensite lamellae and nano-twins in the medium-sized recrystallized grains [58], corresponding to the first stable section (11.7%-15.5% of true strain). In the early stage of transformation, the volume fractions of the HCP-martensite and twins were relatively low, however, the thicknesses of such lamellae structures were very thin (below 100 nm) which could refine the microstructure, thus reducing the mean free path of dislocations [60]. After the special increasing stage, the work hardening rate had a continuous reducing trend in P750C-2m. It could be caused by the less decrease of the mean free path for dislocations by such lamellae due to the growth of lamellae prevailing over the nucleation [58]. In this case the first stable section in the FCC fraction evolution could be related to the nucleation of HCP-martensite process while the while the followed quick decreasing part should represent the HCP phase growth. The final FCC fraction of in the P750C-2m is ~57.7% which is lower than that of the P750C-1m (~64.4%). More HCP-martensite was generated during deformation in the P750C-2m than P750C-1m and then the HCP phase tend to share more load enabling more plastic deformation in the FCC phase, which could contribute to the higher ductility in the P750C-2m. The tensile properties, i.e., tensile strength vs. elongation, of the studied metastable HEAs in comparison with the traditional metallic materials [23, 69-71] are shown in Figure 15 with the schematics of deformation mechanisms. The tensile properties of metastable HEAs treated with different annealing processes form a dash line closer to the right-top corner on the summary map, which means that the studied alloys possess better mechanical properties than the conventional alloys and steels. For the P750C-30s with almost no ductility and high strength, there are no FCC to HCP transformation involved due to the increased stability of the FCC phase by pre-deformed substructures and nano-grains [58]. Because the annealing time was too short to have enough grain recrystallizations and the redistribution and annihilation of dislocations. The samples with a high strength and low ductility have small grain sizes, pre-deformed dislocation densities, and twins. In these samples, FCC to HCP transformation tends to occur at the very large stress. It will leave the HCP phase very limited opportunity to share load from the FCC phase and make the lattice strains of all grain orientations have the right bending behavior during plastic deformation. For the samples with medium strength and ductility, the dislocation density could be reduced by longer annealing time leading to a lower strength. The HCP martensite forms at a medium range of stress, which could share a certain load from the FCC phase, enabling the lattice strain of {311} grain family with a linear trend. The samples at the top area in the figure of elongation vs. tensile strength could have a larger grain size and lower dislocation density leading to a further decrease of strength. In these sample, the FCC to HCP transformation could be triggered early at a relatively low strength which could provide a dramatic multistage work hardening behavior. Given the early contribution to load sharing from the HCP martensite, the lattice strain of {311} grain family in FCC phase tends to have a vertical trend after the phase transformation. Moreover, the R750C-3m and R650-15m have comparable LCF performance compared with other alloys as shown in Figure 16. However, the metastable HEAs possess the highest tensile strengths among the plotted materials, especially the R750C-3m which has a tensile strength of ~1296 MPa. In this case, the metastable HEAs could be designed to have different combinations of strength and ductility without sacrifice of LCF lives.

3.4 Conclusions

In summary, the continuous deformation mechanisms of interstitial metastable HEAs with different tensile properties are revealed in a whole picture via the real-time in situ neutron diffraction. A wide range of strength-ductility tradeoff was obtained by a series of annealing procedures. The multistage work hardening behavior triggered by FCC to HCP transformation could provide a good combination of strength and ductility. The timing for triggering the phase transformation could be tuned by different preparation processes which could provide different deformation mechanisms by changing the load partitioning between FCC matrix and HCP martensite. By tuning the tensile property, the metastable HEAs could obtain a high tensile strength of ~1296 MPa without a sacrifice of the LCF life. This research could contribute to the further design of metastable metallic materials and facilitate the engineering applications of the HEAs.

APPENDIX

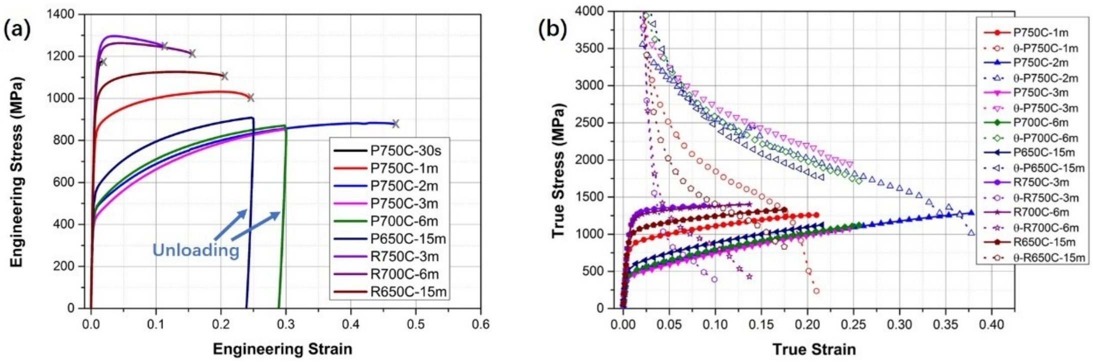

Figure 11. (a) Engineering stress-strain curves of all the samples. (b) True stress-strain curves with corresponding work hardening curves.

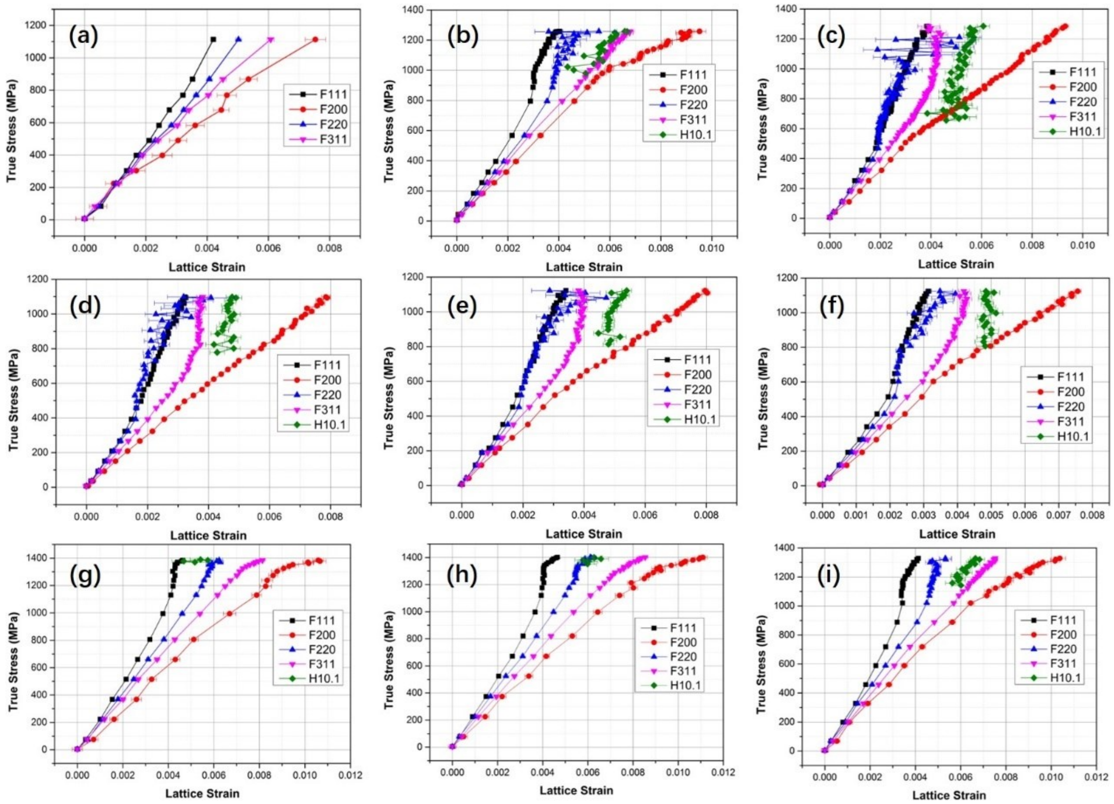

Figure 12. Evolutions of lattice strain of FCC and HCP grain families with macro true stress along the loading direction of different samples: (a) P750C-30s, (b) P750C-1m, (c) P750C-2m, (d) P750C-3m, (e) P700C-6m, (f) P650C-15m, (g) R750C-3m, (h) R700C-6m, (i) R650C-15m.

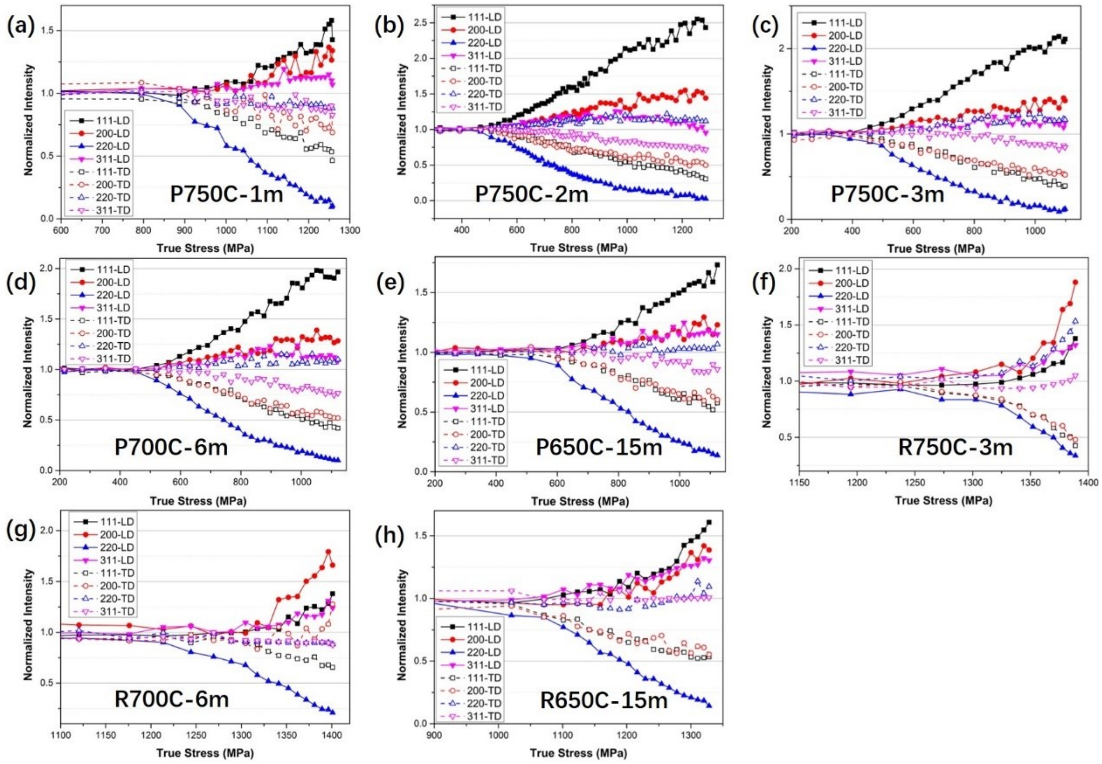

Figure 13. Normalized intensity evolutions of FCC grain families with macro true stress in LD and TD for different samples: (a) P750C-1m, (b) P750C-2m, (c) P750C-3m, (d) P700C-6m, (e) P650C-15m, (f) R750C-3m, (g) R700C-6m, (h) R650C-15m.

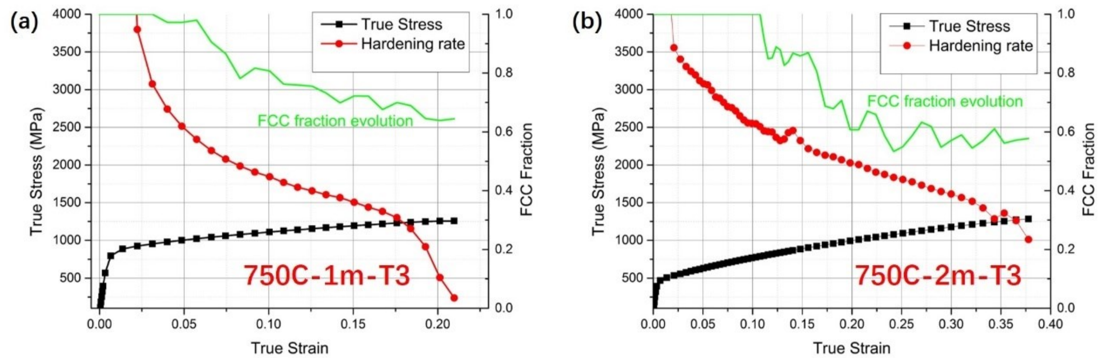

Figure 14. FCC fraction evolutions with corresponding true stress-strain curves and work hardening curves: (a) P750C-1m, (b) P750C-2m.

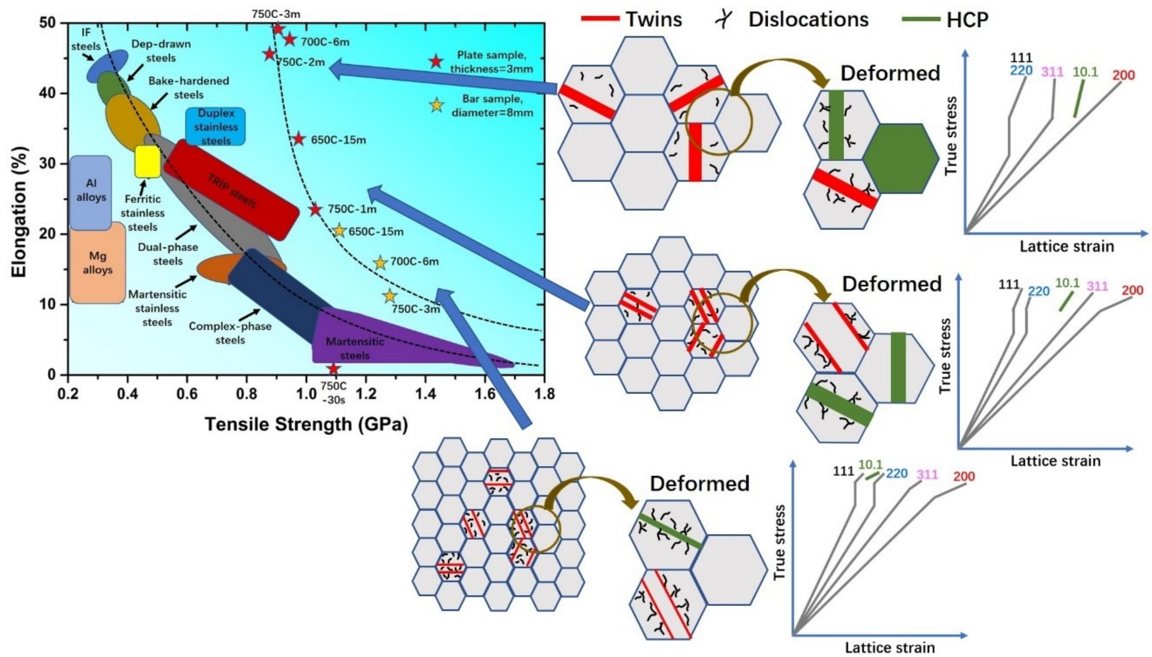

Figure 15. The tensile properties (tensile strength vs. elongation) of the studied interstitial metastable HEAs in comparison with the traditional metallic materials [23, 69-71], with corresponding schematics of different types of deformation mechanisms.

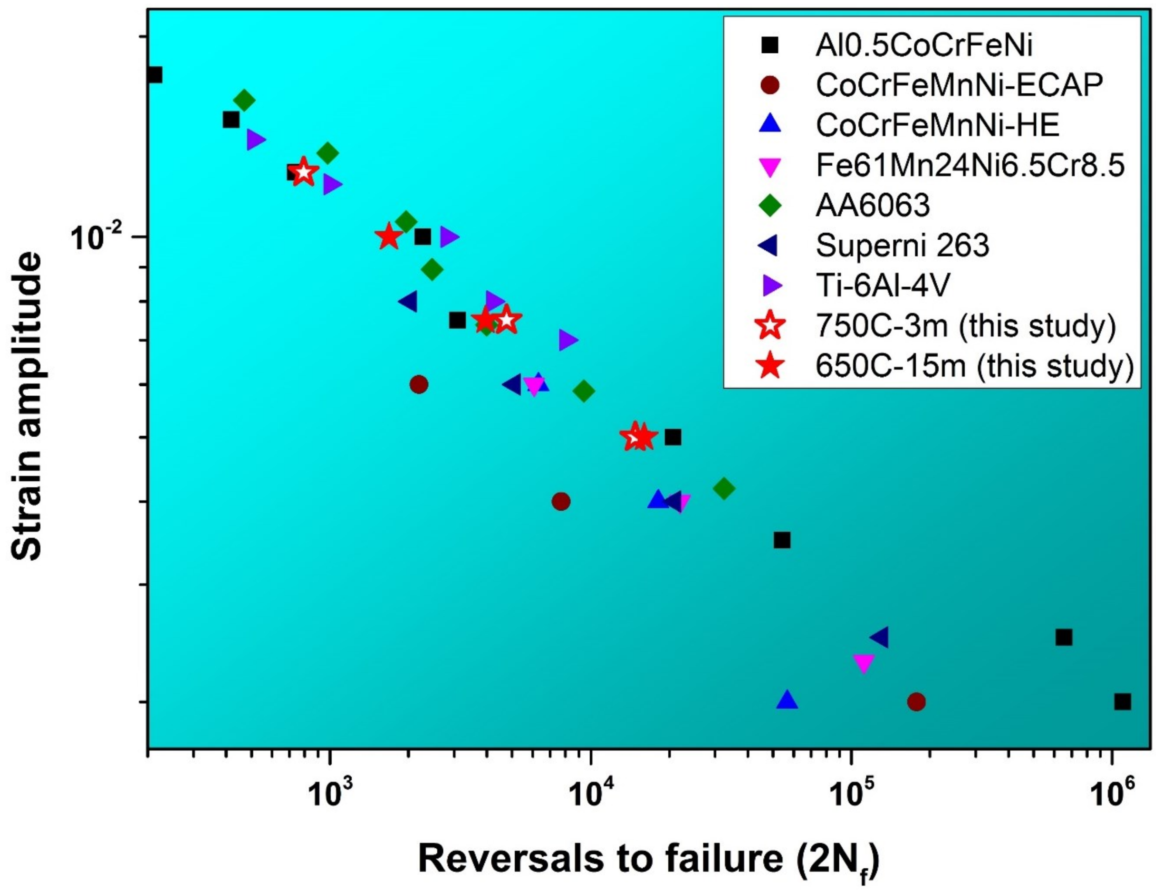

Figure 16. The comparison of low cycle fatigue data for the studied alloys, other HEAs, and conventional alloys [18, 25, 42-45].

CHAPTER 4.
MECHANICAL BEHAVIOR OF MULTICOMPONENT INTERMETALLIC NANOPARTICLE STRENGTHENED HIGH-ENTROPY ALLOY UNDER UNIAXIAL TENSION AND LOW-CYCLE FATIGUE

Abstract

Micro-mechanical behaviors of the multicomponent intermetallic nanoparticles strengthened high entropy alloy was investigated via in situ neutron diffraction during uniaxial tension. The $(FeCoNi)_{86}Al_7Ti_7$ alloy (Al7Ti7) with a high density of $L1_2$ precipitate (size of ~ 100 - 200 nm) was fabricated which showed an excellent combination of tensile strength (~ 1.2 GPa) and ductility (~ 38.5%). A dramatic multistage work hardening behavior was observed during the tensile test which could provide an excellent ductility. The main reasons of the multistage work hardening behavior could be the load sharing of the $L1_2$ precipitate in the early stages (I and II) and the deformation texture induced load transferring back to FCC matrix in the late stages (III and IV). The deformation texture of the $L1_2$ precipitate could be closely related to the slips and/or twinning in this kind of ductile multicomponent intermetallic nanoparticles. Moreover, the low cycle fatigue (LCF) tests of the Al7Ti7 alloy were conducted which indicates that the Al7Ti7 has similar LCF life compared with other materials in the medium strain amplitudes and it could have better LCF performance at high strain amplitudes (>1%) based on the trend prediction.

4.1 Introduction

The strength-ductility trade-off in metallic materials has been extensively investigated for improving the mechanical properties. High entropy alloys (HEAs) [1, 3], also been called as multicomponent alloys, could be a new promising alloying strategy to overcome the trade-off phenomenon [2, 9, 10, 22, 23, 55-57]. Uniform precipitation or secondary phase could be one of the most efficient approaches to improve the strengths HEAs, however, there will be a lot of sacrifice of ductility when the tensile strengths larger than 1100 MPa [72-76]. For example, the FeCoNi alloy, as the base alloy, were studied using oxide dispersion [74] and precipitations [75, 76] to achieve high improved strengths while the values of ductility have obvious decreases. The increase of strength could due to the hindering of dislocation movements by the hard secondary phases [72, 74, 76]. In the same time, the hard secondary phases with intrinsic brittleness could introduce localized stress-strain concentrations and trigger microcracks during loading [77]. Moreover, the sensitivity of the secondary phases to environmental embrittlement could be increased by the high reactive elements, such as Al in the Ni_3Al intermetallic phase which further lower the ductility [78]. Yang et al. [57] proposed to break the strength-ductility trade-off by introducing high-density ductile multicomponent intermetallic nanoparticles (MCINPs) in multicomponent alloys, which show superior strength of ~1500 MPa and ductility of ~50% in tension at room temperature . The excellent ductility in such strong precipitate strengthened HEAs is attributed to triggering a distinctive multistage work-hardening behavior, resulting from pronounced dislocation activities and deformation-induced microbands [57]. However, the real-time and quantitatively continuous deformation mechanism evolutions of the MCINPs strengthened HEAs under loading is still not investigated due to the limitations of the post-test techniques. Because the post-mortem measurements cannot quantitatively provide the load partitioning in different phases and grain orientations and hardly have the ability of tracking activations and evolutions continuously of deformation mechanisms.

In this study, the multicomponent nanoprecipitate strengthened HEA, $(FeCoNi)_{86}Al_7Ti_7$ [57] denoted as Al7Ti7, was fabricated with large sample size for in situ neutron diffraction measurements. The in situ neutron diffraction was performed to investigate the continuous deformation mechanism evolutions of the Al7Ti7 under tension. Different kind of multistage work hardening behavior was observed compared with the literature. Besides the dislocation activities and microbands, the pronounced correlation between L12 precipitate deformation behaviors and the multistage work hardening behavior. Moreover, the low cycle fatigue (LCF) performances of the Al7Ti7 were also tested, which are comparable with the other HEAs and conventional alloys. In this case, the Al7Ti7 tends to possess excellent combination of strengths and ductility without sacrifice of LCF life. This study could fill the blank of the deformation mechanisms of the MCINPs strengthened HEAs and understanding of the role of MCINPs which will be benefit to the further design of high-performance alloys. It could promote the engineering applications of HEAs in the future.

4.2 Experimental

The $(FeCoNi)_{86}Al_7Ti_7$ alloy (at.%) was prepared with pure elements (>99.9% wt.%) by vacuum induction melting and casting. The alloy ingot was homogenized at 1200 °C for 2 h followed by water-quenching. Then cold rolling was conducted with a thickness reduction of ~65%. After that, the alloy ingot was heat treated at 1150 °C for ~1.5 min for recrystallization. The final heat treatment is annealing at 780 °C for 4 h followed by water-quenching. Rod dog-bone samples were machined with the dimensions of Φ6.35*13 mm in gauge section for both tensile and LCF tests.

The transmission electron microscope (TEM) was performed on a ZEISS LIBRA 200 HT FE MC. The TEM samples were prepared by twin-jet polishing with an electrolyte consisting of 95% ethanol and 5% perchloric acid in a volume fraction under −40 °C and voltage of 30 V.

The in situ tensile neutron-diffraction measurements was conducted with an MTS load frame at the VULCAN Engineering Materials Diffractometer [29, 30], the Spallation Neutron Source (SNS), Oak Ridge National Laboratory (ORNL). The fully-reversed strain-controlled LCF tests were performed at different strain amplitudes ($\pm 0.75\%$, $\pm 0.5\%$, $\pm 0.25\%$) with triangular loading waveforms under a continuous-loading condition and the initial loading is in tension. The strain rate for the LCF is $0.01 s^{-1}$.

The in situ neutron diffraction data were analyzed using the VULCAN Data Reduction and Interactive Visualization software (VDRIVE) [31]. The evolution of the dislocation density is studied via the relationship between the dislocation density of a specific lattice plane and its full width at half maximum (FWHM) of the diffraction peak described by the equation [32, 33].

4.3 Results and Discussions

The microstructure of the Al7Ti7 by TEM is shown in Figure 17. High density of cuboidal $L1_2$ precipitates with the size ~ 100-200 nm are generated in the FCC matrix in the Al7Ti7. The $L1_2$ particle size is larger than that in the literature [57], ~30-50 nm. The growth of the precipitate tends to have a preferred orientation along the <200> of the FCC matrix. This kind of multicomponent $L1_2$ particle with the composition of $Fe_{10.06}Co_{23.69}Ni_{43.23}Al_{8.61}Ti_{14.41}$ shows remarkable strain hardening ability (~2.1 GPa) and excellent ductility of ~40% [57].

The studied Al7Ti7 has the yield strength and ultimate tensile strength of 893 MPa and 1205 MPa, respectively, with the ductility of ~38.5%, as shown in Figure 18. To further understand the mechanical behavior, the work hardening rate evolution is plotted in Figure 19. The Al7Ti7 shows a multistage work hardening behavior during tension and there could be four stages to describe the whole deformation behavior. Stage I (true strain < ~ 2%) has a fast decrease of work hardening rate and it is usually related to the dislocation rearrangement [60]. In stage II (true strain of ~ 2-5.17%), the decrease of work hardening rate slows down and turn into an increase part. The stage III (true strain of ~ 5.17-10.1%) and IV (true strain of > ~ 10.1%) have a continuous decrease of the work hardening rate and the slope of stage IV is lower than Stage III. The necking point is predicted to happen at ~18.5% of true stress.

In order to understand the underlying deformation mechanisms, the lattice strain evolutions of the FCC and $L1_2$ phases with different grain orientations are plotted in Figure 20 with the corresponding work hardening stages marked. The stage I contains the whole linear increasing part of the lattice strain and the first turn of each grain family. In this stage, the FCC (200) shows an obvious right turn which means the FCC (200) grain family tends to share more load. In the same time, the FCC (111) (220) (222) have the upward trends. During the transition from stage I to II, the grain families of $L1_2$ phase start to take the load sharing from the FCC matrix with a right bend of the lattice strain. In this way, the FCC (200) (311) tend to show upward turns in stage II and early stage III. In the middle of stage III, surprisingly, the FCC (200) has a second right turn, which mean the FCC phase starts to take load sharing again. In this part, the (210) of $L1_2$ phase tends to reduce the load sharing due to the gradual vanishing of the $L1_2$ (210) grain orientation along loading direction (LD). As shown in the Figure 21, the peak of the $L1_2$ (210) grain orientation in LD gradually cannot be detected during loading while the (210) in TD could be seen during the whole process of loading and unloading. In the same time, the $L1_2$ (211) peaks can be seen in both LD and TD for the whole process.

The normalized intensity evolutions of the grain families for $L1_2$ precipitate is shown in Figure 22. The normalized intensity of $L1_2$ (210) in LD decreases fast after 1000 MPa while that in TD increases gradually. This could relate to the deformation texture with $L1_2$ (210) grain orientation favored in TD. The deformation texture could be caused by slips and/or twinning of the $L1_2$ particle as well as the grain rotations. For the normalized intensity evolutions in FCC phase, as shown in Figure 23 (a), most of the grain orientations in LD have an increasing trend except for the FCC (220). The normalized intensity of FCC (220) increases in TD and decreases in LD, which indicate that the deformation texture with the FCC (220) grain orientation favored in TD occurred during loading. In the same time, the FCC (111) (200) (222) grain orientations are favored in LD during deformation. In Figure 23 (b), the normalized intensity evolutions of FCC (111) and (222) are plotted in a certain range of stresses to have a clear observation. At the stress of ~1030 MPa, the normalized intensity of FCC (111) in TD begin to have different trend with that in LD. The normalized intensity of FCC (111) in TD shows a plateau trend during the stress range of ~1030-1160 MPa while that in LD keeps an obvious increasing trend. Beyond the stress of ~1160 MPa, the normalized intensity of FCC (111) in TD starts to decrease. Similar phenomenon is also observed for the FCC (222) grain family. It suggests that, during the deformation with the stress range of ~1030-1160 MPa, the more and more FCC (111) and (222) grain orientations involved in LD while those in TD are in a steady condition. The strong increasing deformation texture of $L1_2$ precipitate in TD could somehow postpone the decrease of normalized intensities of the FCC grain orientations, since the $L1_2$ precipitate has the diffraction peak overlapping with the FCC matrix. It is worth to mention that the stress range of ~1030-1160 MPa is almost corresponding to the stage II of work hardening behavior.

The FWHM evolutions in LD are shown in Figure 24 marked with the corresponding sections of the work hardening stages. The FWHM values of the FCC (200) and (311) have a relatively steady slope of increasing after the stress reaching ~1000 MPa which could be related to the stable accumulation of dislocation in these grain orientations. Meanwhile, the values of FWHM of $L1_2$ (210) and (211) have much smaller increase compared with the FCC grain orientations which means that the dislocation density accumulations could keep in a low level in $L1_2$ (210) and (211). It indicates that more dislocation generations and movements exist in the FCC matrix than in the $L1_2$ precipitate during the deformation. There is more plastic strain concentrates in the FCC matrix than in the $L1_2$ precipitate. For the FWHM evolutions of the FCC (222), there is a similar multistage behavior can be observed which is corresponding to the multistage work hardening behavior, as shown in Figure 25. The increasing rate of FWHM with the stress larger than ~1000 MPa in the FCC (222) decreases stage by stage which could indicate that the dislocation accumulation tends to slow down in the stages of III and IV. The quick increasing of dislocation density in the FCC (222) after 1000 MPa (~stage II) could be caused by the load sharing transferred from FCC matrix to $L1_2$ precipitate which allows the FCC phase to have more plastic deformations. The first decrease of the dislocation accumulation rate happens in stage III and this could result from the gradual deformation texture which reduces the load sharing of $L1_2$ precipitate in LD and lets the FCC phase start to share the load again with less plastic deformations. In stage IV, the rate of dislocation accumulation decreases again which could be caused by a certain load sharing transferred back to FCC matrix and the existing dislocations with a high density. In this way, the load sharing of the $L1_2$ precipitate and the deformation texture induced load transferring back to FCC matrix are the main reasons for the multistage work hardening behavior of the Al7Ti7 HEA in this work.

The studied Al7Ti7 HEA have great improvements in both strengths and ductility compared with the FeCoNi HEA (base alloy) [79]. However, the strengths and ductility of Al7Ti7 in this work are not as high as those of Al7Ti7 from literature [57]. In terms of strength, the large sized particles (~ 100 – 200 nm) in this work could be easier to have slips or twinning than the small particles (~ 30 – 50 nm) in the literature [57], which leads to the limited precipitation strengthening effect in the studied Al7Ti7. The larger particles also could have stronger load sharing in the early deformation stage, which makes the plastic strain concentration happen in FCC matrix leading to a remarkable strain hardening behavior. For particles with smaller sizes in a certain extent, they may have relatively lower load partitioning effect in the early stage of deformation, which could slow down the strain hardening in FCC matrix and then make more contributions to the ductility.

The comparison of tensile property of the studied Al7Ti7 HEA, the alloys from Task 2, and other conventional metallic materials [23, 69-71] is shown in Figure 26. The Al7Ti7 HEA locates at the place nearest to the top-right corner than other materials which indicated that it has the best tensile property among these materials. In Figure 27, the comparison of LCF performance of the studied Al7Ti7 HEA, some other HEAs alloys [18, 25], and some conventional metallic materials [42-45]. The Al7Ti7 HEA shows a comparable LCF life in comparison with other materials in the medium strain amplitudes (±0.5% and ±0.75%) and it could have better LCF performance at high strain amplitudes (>1%) based on the drawing trend.

4.4 Conclusions

To sum up, the large sized sample of MCINPs strengthened HEA, $(FeCoNi)_{86}Al_7Ti_7$, is fabricated and tested via in situ neutron diffraction for the continuous deformation mechanisms. The alloy shows a multistage work hardening behavior during tension which could facilitate the ductility of the strengthened HEA. The multistage work hardening behavior could be caused by the load sharing transferred between the $L1_2$ precipitate and the FCC matrix. Moreover, the MCINPs strengthened HEA shows a comparable LCF life compared with other metallic materials in the medium strain amplitudes. It indicates that MCINPs could highly strengthen the HEAs with sacrifice of the LCF life. This work could further promote the industrial applications of HEAs.

APPENDIX

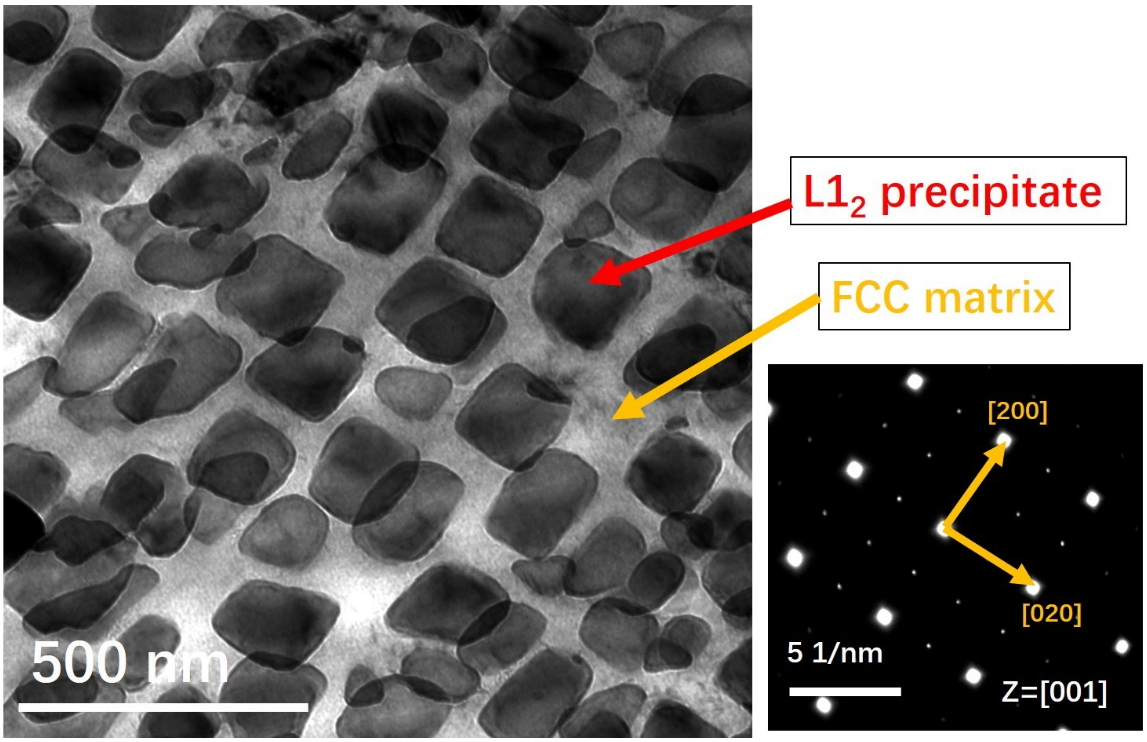

Figure 17. The microstructure image by TEM of the Al7Ti7.

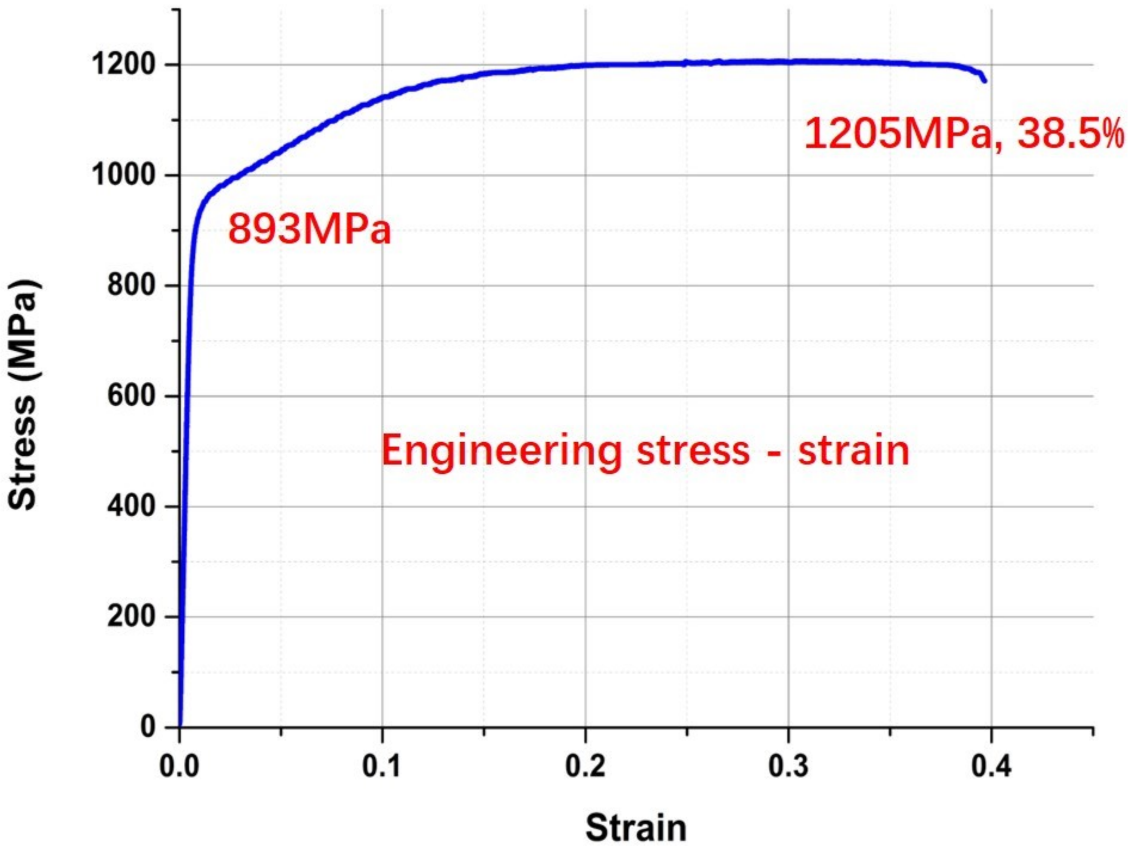

Figure 18. The engineering stress-strain curve of the Al7Ti7.

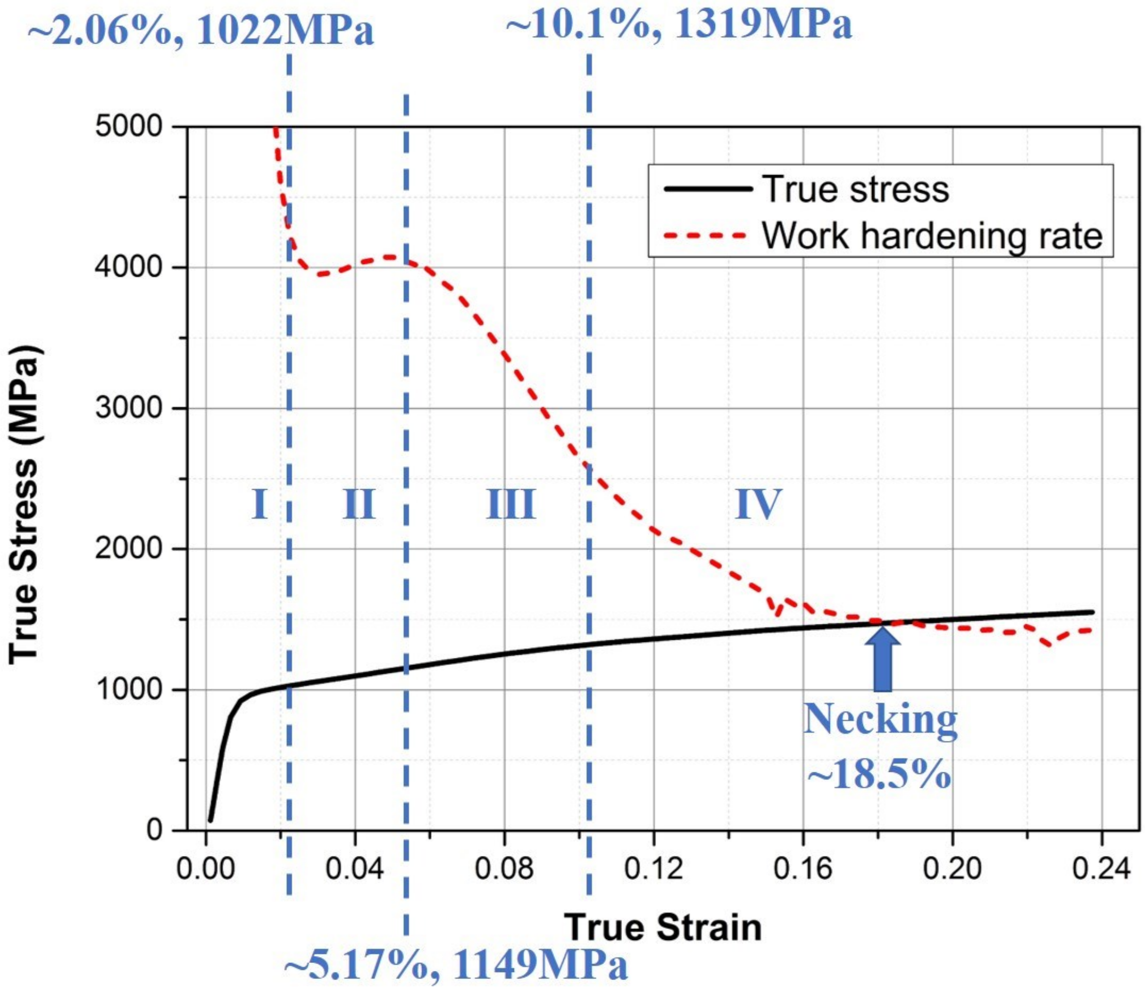

Figure 19. The work hardening behavior with true stress-strain curve of the Al7Ti7.

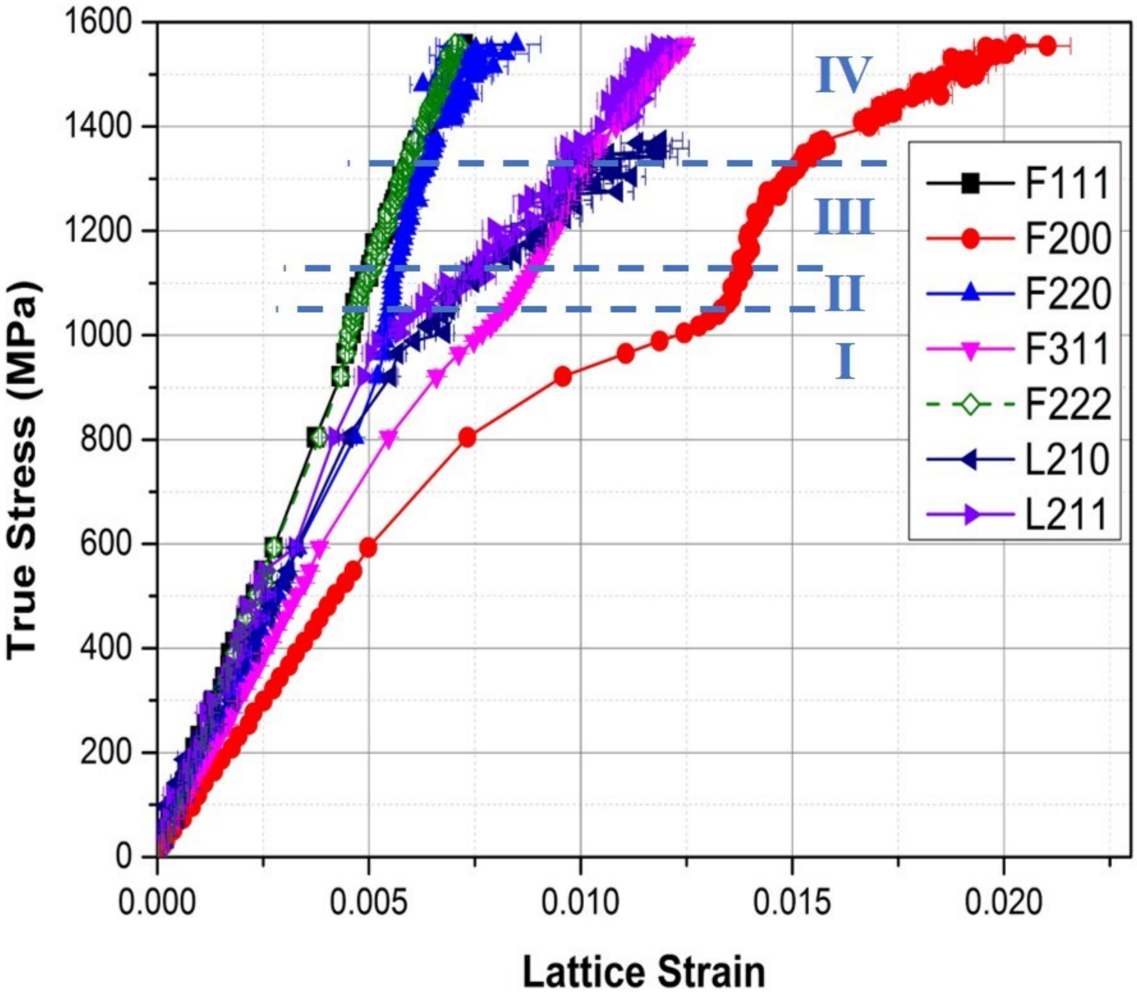

Figure 20. Lattice strain evolutions of the Al7Ti7.

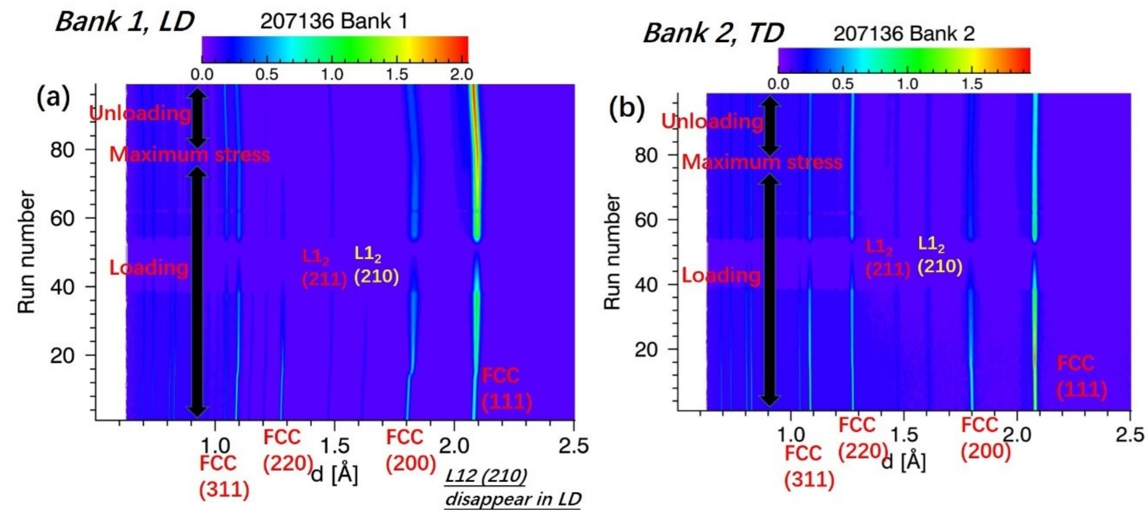

Figure 21. 2D view of the in-situ tension neutron data of the Al7Ti7.

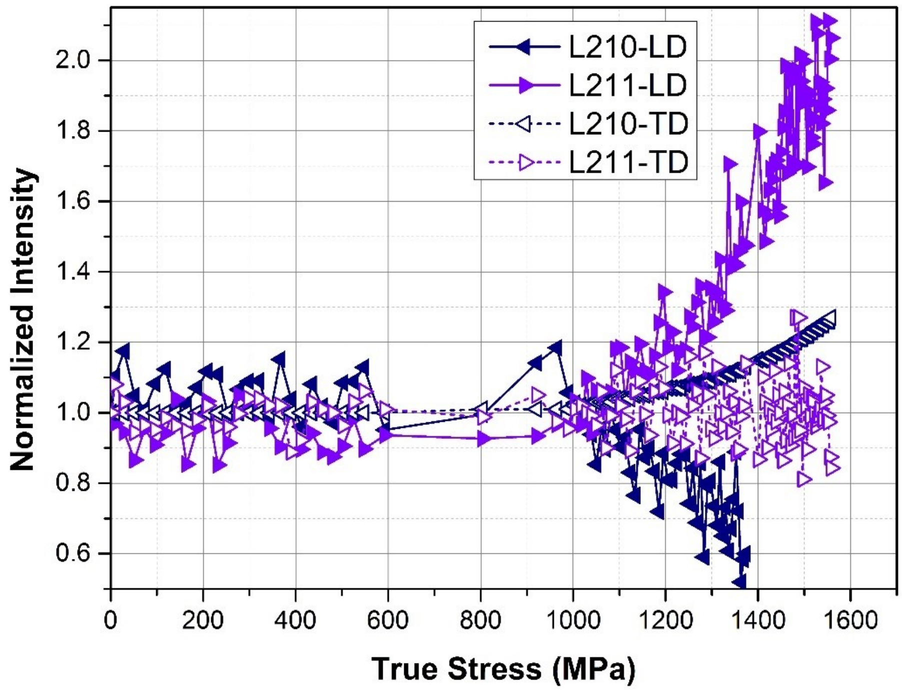

Figure 22. Normalized intensity of the $L1_2$ precipitate in the Al7Ti7.

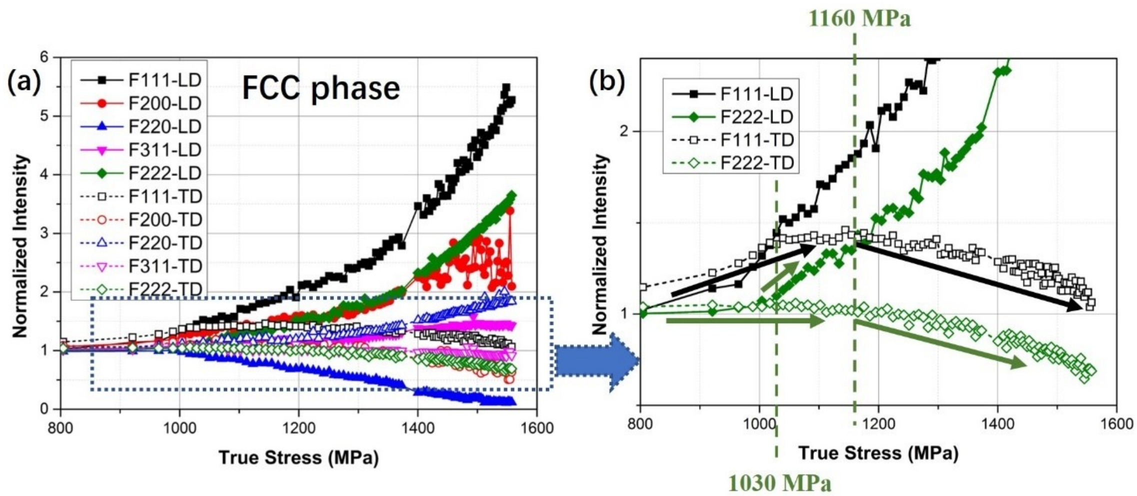

Figure 23. Normalized intensity of the FCC matrix in the Al7Ti7.

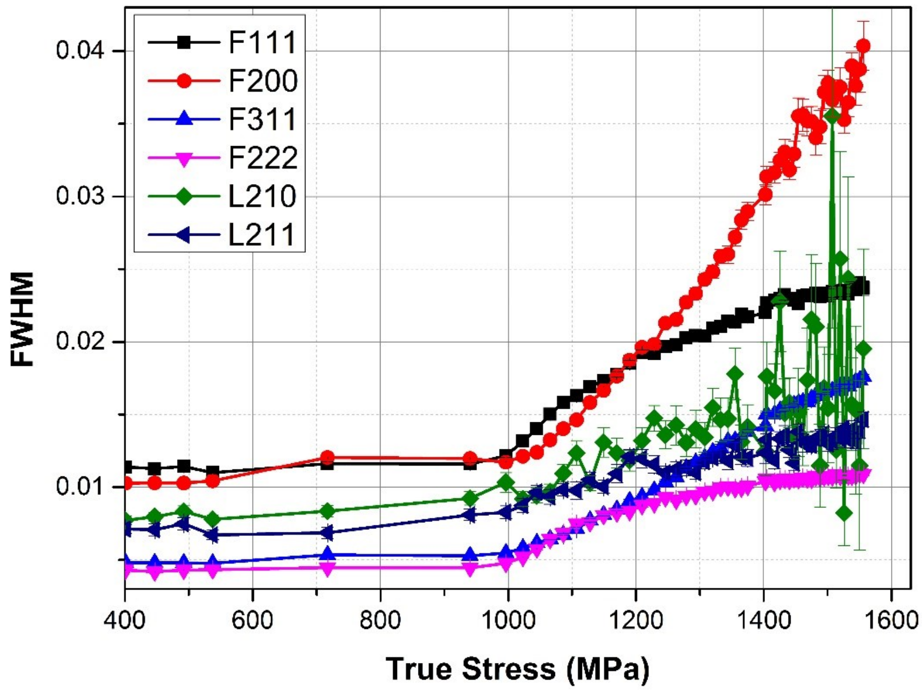

Figure 24. The FWHM evolutions of the Al7Ti7.

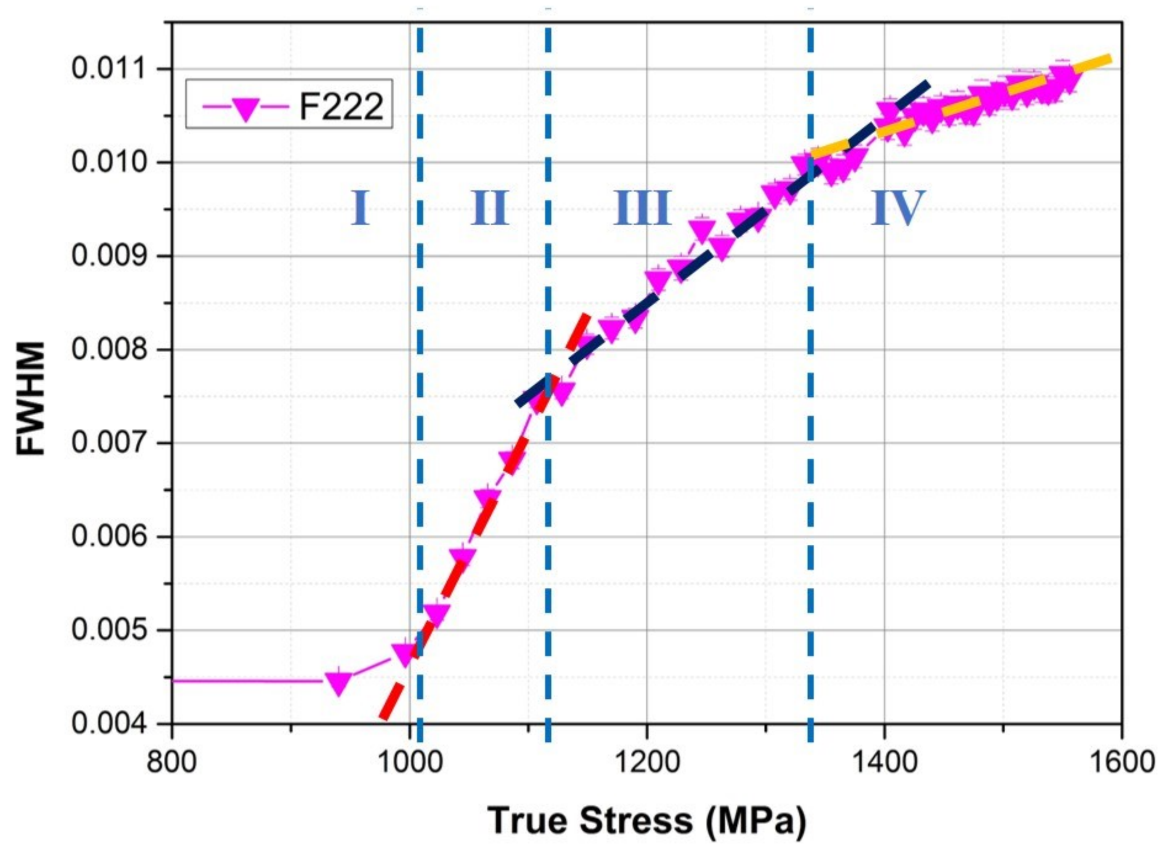

Figure 25. The multistage FWHM evolutions of FCC (222) at high stresses in the Al7Ti7.

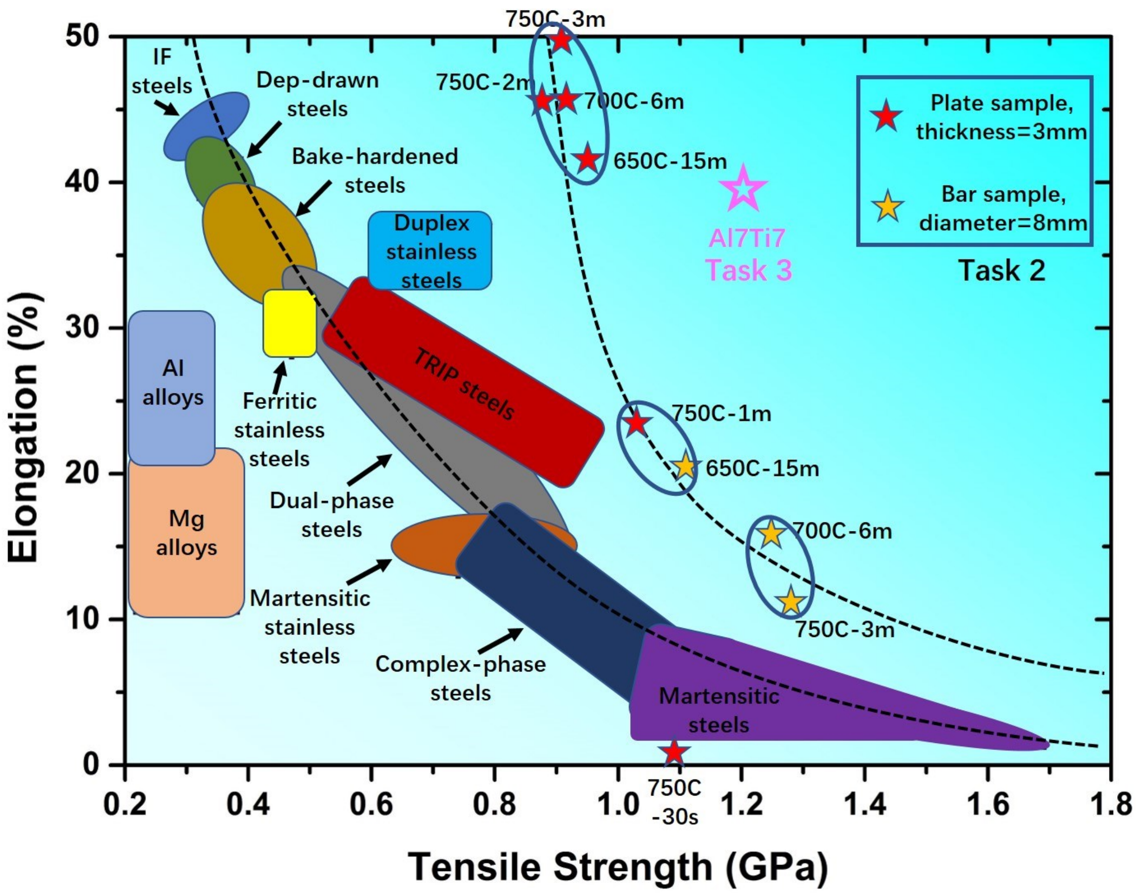

Figure 26. Tensile properties of the studied Al7Ti7 HEA in comparison with the HEAs in Task 2 and the traditional metallic materials [23, 69-71].

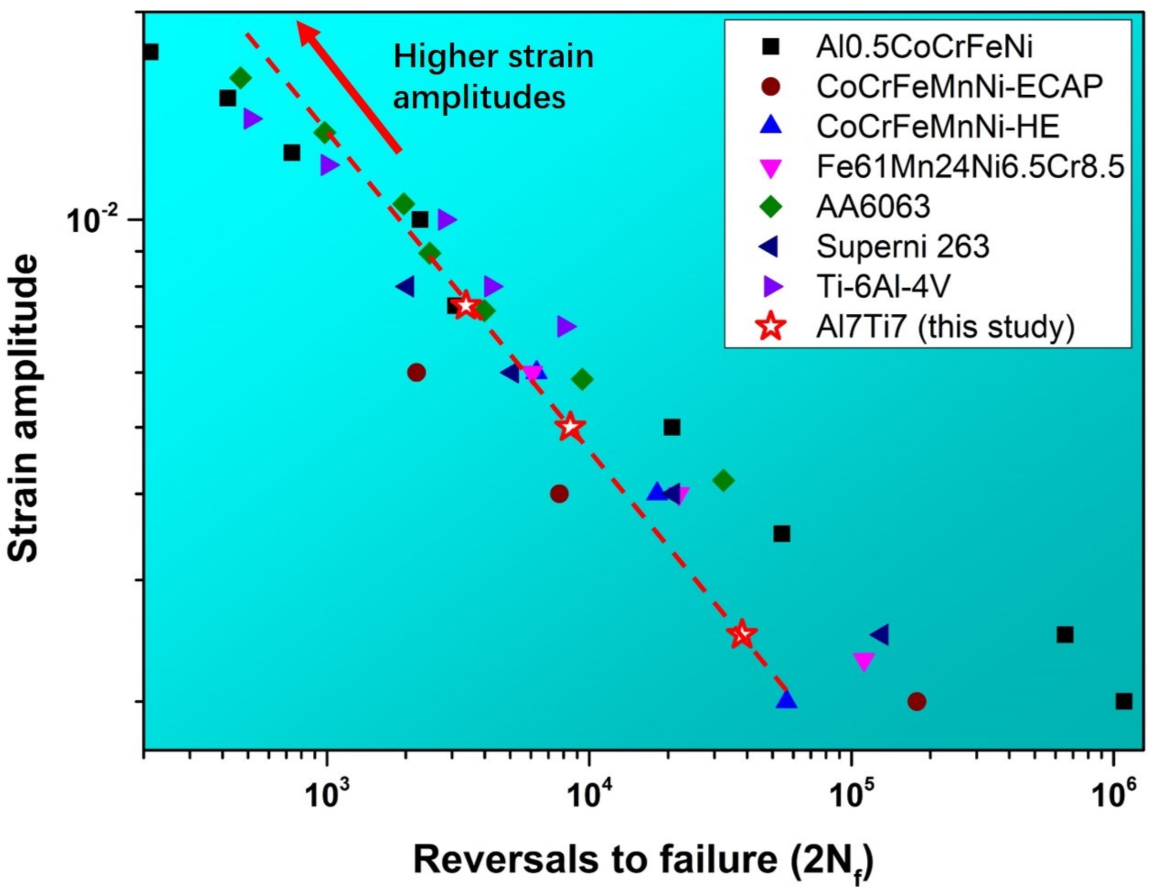

Figure 27. LCF performances of the Al7Ti7 in comparison with some other HEAs and the traditional metallic materials [18, 25, 42-45].

CHAPTER 5. CONCLUSIONS AND FUTURE SUGGESTIONS

5.1 Conclusions

Seeking for stronger alloys with excellent fatigue properties is one of the core topics for the industrial applications. The proposed research combined the in situ neutron diffraction and micromechanical modeling to reveal the fatigue mechanism of the LCF of incoherent precipitate strengthened HEAs. The whole picture of deformation mechanism evolutions of the interstitial HEA under uniaxial tension was investigated and provide a series of mechanical properties which are superior to most of the conventional alloys and steels. High strengths and good LCF performances of HEAs were achieved by introducing coherent nanoparticles and phase transformations. The deformation mechanisms of the studied HEAs could be quantitatively explained with the help of in-situ neutron diffraction measurements. Coherent nanoparticles and metastable phases could be the efficient methods to promote fatigue resistance of HEAs, which could further facilitate the industrial application of HEAs.

5.2 Future Suggestions

In this work, the multicomponent nanoparticles and phase transformations are used to develop the HEAs with excellent strengths and good fatigue resistance. However, there are some future suggestions on this research which could facilitate the fundamental understanding and industrial applications of the HEAs with nanoparticles and metastable phases. The future suggestions are shown below.

(1) In this work, several compositions of HEAs were studied for the deformation mechanisms in tension and LCF performances. More future investigations could be done on the alloy design of HEAs, such as high-throughput design, for optimizing metastable phases and nanoparticles, which could be beneficial to the developments of stronger alloys with excellent fatigue resistance.

(2) The quantitative understanding of the deformation mechanisms in tension and LCF is still limited for the HEAs with metastable phases and multicomponent nanoparticles. More micro-mechanical models are expected in the future which can fit the experimental data well and help to predict the mechanical properties of high-performance HEAs.

(3) Further investigation on the deformation mechanisms of the multicomponent nanoprecipitates in HEAs could been done by TEM. It is also worth to fabricate the sample with the composition of the ductile multicomponent intermetallic nanoprecipitate for in-situ neutron diffraction study.

(4) The sizes of multicomponent nanoprecipitates could be tuned to adjust the strain concentrations in the FCC matrix, which may optimize the combination of strength and

ductility. In situ neutron diffraction study on the small-sized nanoparticle strengthened HEAs for the deformation mechanisms of the nanoparticle and the matrix could be used to have a better understanding of the precipitate size effects.

(5) Tuning the initial microstructures of MTHEAs with different heat treatments could be a promising method to develop the materials with ultra-high yield strengths without a sacrifice of the LCF life.

REFERENCES

[1] B. Cantor, I.T.H. Chang, P. Knight, A.J.B. Vincent, Microstructural development in equiatomic multicomponent alloys, Materials Science and Engineering: A 375-377 (2004) 213-218.

[2] E.P. George, D. Raabe, R.O. Ritchie, High-entropy alloys, Nature Reviews Materials 4(8) (2019) 515-534.

[3] J.W. Yeh, S.K. Chen, S.J. Lin, J.Y. Gan, T.S. Chin, T.T. Shun, C.H. Tsau, S.Y. Chang, Nanostructured high-entropy alloys with multiple principal elements: Novel alloy design concepts and outcomes, Adv Eng Mater 6(5) (2004) 299-303.

[4] J.W. Yeh, Alloy design strategies and future trends in high-entropy alloys, JOM 65(12) (2013) 1759-1771.

[5] D.B. Miracle, O.N. Senkov, A critical review of high entropy alloys and related concepts, Acta Materialia 122 (2017) 448-511.

[6] H.Y. Diao, R. Feng, K.A. Dahmen, P.K. Liaw, Fundamental deformation behavior in high-entropy alloys: An overview, Current Opinion in Solid State and Materials Science 21(5) (2017) 252-266.

[7] Y. Zhang, Y.J. Zhou, J.P. Lin, G.L. Chen, P.K. Liaw, Solid-Solution Phase Formation Rules for Multi-component Alloys, Advanced Engineering Materials 10(6) (2008) 534-538.

[8] L.J. Santodonato, Y. Zhang, M. Feygenson, C.M. Parish, M.C. Gao, R.J. Weber, J.C. Neuefeind, Z. Tang, P.K. Liaw, Deviation from high-entropy configurations in the atomic distributions of a multi-principal-element alloy, Nature communications 6 (2015) 5964.

[9] Z. Li, K.G. Pradeep, Y. Deng, D. Raabe, C.C. Tasan, Metastable high-entropy dual-phase alloys overcome the strength-ductility trade-off, Nature 534(7606) (2016) 227-30.

[10] Z. Lei, X. Liu, Y. Wu, H. Wang, S. Jiang, S. Wang, X. Hui, Y. Wu, B. Gault, P. Kontis, D. Raabe, L. Gu, Q. Zhang, H. Chen, H. Wang, J. Liu, K. An, Q. Zeng, T.G. Nieh, Z. Lu, Enhanced strength and ductility in a high-entropy alloy via ordered oxygen complexes, Nature 563(7732) (2018) 546-550.

[11] B. Gludovatz, A. Hohenwarter, D. Catoor, E.H. Chang, E.P. George, R.O. Ritchie, A fracture-resistant high-entropy alloy for cryogenic applications, Science 345(6201) (2014) 1153-1158.

[12] M.A. Hemphill, T. Yuan, G.Y. Wang, J.W. Yeh, C.W. Tsai, A. Chuang, P.K. Liaw, Fatigue behavior of Al0.5CoCrCuFeNi high entropy alloys, Acta Materialia 60(16) (2012) 5723-5734.

[13] O.N. Senkov, J.D. Miller, D.B. Miracle, C. Woodward, Accelerated exploration of multi-principal element alloys with solid solution phases, Nature communications 6 (2015) 6529.

[14] H. Huang, Y. Wu, J. He, H. Wang, X. Liu, K. An, W. Wu, Z. Lu, Phase-transformation ductilization of brittle high-entropy alloys via metastability engineering, Advanced materials (1701678) (2017) 1-7.

[15] Y. Lu, X. Gao, L. Jiang, Z. Chen, T. Wang, J. Jie, H. Kang, Y. Zhang, S. Guo, H. Ruan, Y. Zhao, Z. Cao, T. Li, Directly cast bulk eutectic and near-eutectic high entropy alloys with balanced strength and ductility in a wide temperature range, Acta Materialia 124 (2017) 143-150.

[16] C. Lee, G. Song, M.C. Gao, R. Feng, P. Chen, J. Brechtl, Y. Chen, K. An, W. Guo, J.D. Poplawsky, S. Li, A.T. Samaei, W. Chen, A. Hu, H. Choo, P.K. Liaw, Lattice distortion in a strong and ductile refractory high-entropy alloy, Acta Materialia 160 (2018) 158-172.

[17] Y.J. Liang, L. Wang, Y. Wen, B. Cheng, Q. Wu, T. Cao, Q. Xiao, Y. Xue, G. Sha, Y. Wang, Y. Ren, X. Li, L. Wang, F. Wang, H. Cai, High-content ductile coherent nanoprecipitates achieve ultrastrong high-entropy alloys, Nature communications 9(1) (2018) 4063.

[18] R. Feng, Y. Rao, C. Liu, X. Xie, D. Yu, Y. Chen, M. Ghazisaeidi, T. Ungar, H. Wang, K. An, P.K. Liaw, Enhancing fatigue life by ductile-transformable multicomponent B2 precipitates in a high-entropy alloy, Nature communications 12(1) (2021) 3588.

[19] Z. Tang, T. Yuan, C.-W. Tsai, J.-W. Yeh, C.D. Lundin, P.K. Liaw, Fatigue behavior of a wrought Al 0.5 CoCrCuFeNi two-phase high-entropy alloy, Acta Materialia 99 (2015) 247-258.

[20] Q. Ding, Y. Zhang, X. Chen, X. Fu, D. Chen, S. Chen, L. Gu, F. Wei, H. Bei, Y. Gao, M. Wen, J. Li, Z. Zhang, T. Zhu, R.O. Ritchie, Q. Yu, Tuning element distribution, structure and properties by composition in high-entropy alloys, Nature 574(7777) (2019) 223-227.

[21] S. Wei, S.J. Kim, J. Kang, Y. Zhang, Y. Zhang, T. Furuhara, E.S. Park, C.C. Tasan, Natural-mixing guided design of refractory high-entropy alloys with as-cast tensile ductility, Nat Mater 19(11) (2020) 1175-1181.

[22] Q. Pan, L. Zhang, R. Feng, Q. Lu, K. An, A.C. Chuang, J.D. Poplawsky, P.K. Liaw, L. Lu, Gradient cell–structured high-entropy alloy with exceptional strength and ductility, Science 374(6570) (2021) 984-989.

[23] P. Shi, R. Li, Y. Li, Y. Wen, Y. Zhong, W. Ren, Z. Shen, T. Zheng, J. Peng, X. Liang, P. Hu, Hierarchical crack buffering triples ductility in eutectic herringbone high-entropy alloys, Science 373(6557) (2021) 912-918.

[24] S.A.A. Shams, G. Jang, J.W. Won, J.W. Bae, H. Jin, H.S. Kim, C.S. Lee, Low-cycle fatigue properties of CoCrFeMnNi high-entropy alloy compared with its conventional counterparts, Materials Science and Engineering: A 792 (2020) 139661.

[25] S. Picak, T. Wegener, S.V. Sajadifar, C. Sobrero, J. Richter, H. Kim, T. Niendorf, I. Karaman, On the low-cycle fatigue response of CoCrNiFeMn high entropy alloy with ultra-fine grain structure, Acta Materialia 205 (2021).

[26] S.A.A. Shams, G. Kim, J.W. Won, J.N. Kim, H.S. Kim, C.S. Lee, Effect of grain size on the low-cycle fatigue behavior of carbon-containing high-entropy alloys, Materials Science and Engineering: A 810 (2021).

[27] K. Hockauf, M.F.X. Wagner, T. Halle, T. Niendorf, M. Hockauf, T. Lampke, Influence of precipitates on low-cycle fatigue and crack growth behavior in an ultrafine-grained aluminum alloy, Acta Materialia 80 (2014) 250-263.

[28] J. Xu, Z. Huang, L. Jiang, Effect of heat treatment on low cycle fatigue of IN718 superalloy at the elevated temperatures, Materials Science and Engineering: A 690 (2017) 137-145.

[29] X.L. Wang, T.M. Holden, G.Q. Rennich, A.D. Stoica, P.K. Liaw, H. Choo, C.R. Hubbard, VULCAN—The engineering diffractometer at the SNS, Physica B: Condensed Matter 385-386 (2006) 673-675.

[30] K. An, H.D. Skorpenske, A.D. Stoica, D. Ma, X.-L. Wang, E. Cakmak, First In Situ Lattice Strains Measurements Under Load at VULCAN, Metallurgical and Materials Transactions A 42(1) (2010) 95-99.

[31] K. An, VDRIVE-Data reduction and interactive visualization software for event mode neutron diffraction, ORNL Report, Oak Ridge National Laboratory, ORNL-TM-2012-621 (2012).

[32] T. Ungár, I. Dragomir, Á. Révész, A. Borbély, The contrast factors of dislocations in cubic crystals: the dislocation model of strain anisotropy in practice, Journal of Applied Crystallography 32 (1999) 992-1002.

[33] T. Ungár, J. Gubicza, G. Ribárik, A. Borbély, Crystallite size distribution and dislocation structure determined by diffraction profile analysis: principles and practical application to cubic and hexagonal crystals, Journal of Applied Crystallography 34 (2001) 298-310.

[34] A.S. Tirunilai, T. Hanemann, C. Reinhart, V. Tschan, K.P. Weiss, G. Laplanche, J. Freudenberger, M. Heilmaier, A. Kauffmann, Comparison of cryogenic deformation of the concentrated solid solutions CoCrFeMnNi, CoCrNi and CoNi, Materials Science and Engineering: A 783 (2020).

[35] H.Y. Yasuda, K. Shigeno, T. Nagase, Dynamic strain aging of Al 0.3 CoCrFeNi high entropy alloy single crystals, Scripta Materialia 108 (2015) 80-83.

[36] W. Wei, Y. Feng, L. Han, Q. Zhang, J. Zhang, Cyclic hardening and dynamic strain aging during low-cycle fatigue of Cr-Mo tempered martensitic steel at elevated temperatures, Materials Science and Engineering: A 734 (2018) 20-26.

[37] V. Shankar, A. Kumar, K. Mariappan, R. Sandhya, K. Laha, A.K. Bhaduri, N. Narasaiah, Occurrence of dynamic strain aging in Alloy 617M under low cycle fatigue loading, International Journal of Fatigue 100 (2017) 12-20.

[38] Y.-H. Lin, K.-H. Hu, F.-H. Kao, S.-H. Wang, J.-R. Yang, C.-K. Lin, Dynamic strain aging in low cycle fatigue of duplex titanium alloys, Materials Science and Engineering: A 528(13-14) (2011) 4381-4389.

[39] H. Zhou, Y. He, H. Zhang, Y. Cen, Influence of dynamic strain aging pre-treatment on the low-cycle fatigue behavior of modified 9Cr–1Mo steel, International Journal of Fatigue 47 (2013) 83-89.

[40] G. Sudhakar Rao, J.K. Chakravartty, N. Saibaba, G.S. Mahobia, K. Chattopadhyay, N.C. Santhi Srinivas, V. Singh, Disappearance and reappearance of serrated plastic flow under cyclic loading: A study of dislocation substructures, Materials Science and Engineering: A 603 (2014) 114-120.

[41] S. Hong, K. Lee, S. Lee, Dynamic strain aging effect on the fatigue resistance of type 316L stainless steel, International Journal of Fatigue 27(10-12) (2005) 1420-1424.

[42] H.G. Lambers, C.J. Rüsing, T. Niendorf, D. Geissler, J. Freudenberger, H.J. Maier, On the low-cycle fatigue response of pre-strained austenitic Fe61Mn24Ni6.5Cr8.5 alloy showing TWIP effect, International Journal of Fatigue 40 (2012) 51-60.

[43] S. Nandy, A.P. Sekhar, T. Kar, K.K. Ray, D. Das, Influence of ageing on the low cycle fatigue behaviour of an Al–Mg–Si alloy, Philosophical Magazine 97(23) (2017) 1978-2003.

[44] H. Xu, D. Ye, L. Mei, A study of the back stress and the friction stress behaviors of Ti-6Al-4V alloy during low cycle fatigue at room temperature, Materials Science and Engineering: A 700 (2017) 530-539.

[45] J. Jadav, K.V. Rajulapati, K.B.S. Rao, N.E. Prasad, R. Mythili, K. Prasad, Strain controlled isothermal low cycle fatigue life, deformation and fracture characteristics of Superni 263 superalloy, Materials Science and Engineering: A 760 (2019) 296-315.

[46] S. Huang, D.W. Brown, B. Clausen, Z. Teng, Y. Gao, P.K. Liaw, In Situ Neutron-Diffraction Studies on the Creep Behavior of a Ferritic Superalloy, Metallurgical and Materials Transactions A 43(5) (2011) 1497-1508.

[47] H. Qiao, S.R. Agnew, P.D. Wu, Modeling twinning and detwinning behavior of Mg alloy ZK60A during monotonic and cyclic loading, International Journal of Plasticity 65 (2015) 61-84.

[48] G. Sudhakar Rao, J.K. Chakravartty, S. Nudurupati, G.S. Mahobia, K. Chattopadhyay, N.C. Santhi Srinivas, V. Singh, Low cycle fatigue behavior of Zircaloy-2 at room temperature, Journal of Nuclear Materials 441(1-3) (2013) 455-467.

[49] P. Lukáš, L. Kunz ‡, Role of persistent slip bands in fatigue, Philosophical Magazine 84(3-5) (2004) 317-330.

[50] H. Mughrabi, Cyclic Slip Irreversibilities and the Evolution of Fatigue Damage, Metallurgical and Materials Transactions B 40(4) (2009) 431-453.

[51] Z.F. Zhang, Z.G. Wang, Dependence of intergranular fatigue cracking on the interactions of persistent slip bands with grain boundaries, Acta Materialia 51(2) (2003) 347-364.

[52] M.D. Sangid, The physics of fatigue crack initiation, International Journal of Fatigue 57 (2013) 58-72.

[53] M.D. Sangid, H.J. Maier, H. Sehitoglu, An energy-based microstructure model to account for fatigue scatter in polycrystals, Journal of the Mechanics and Physics of Solids 59(3) (2011) 595-609.

[54] M.D. Sangid, H.J. Maier, H. Sehitoglu, A physically based fatigue model for prediction of crack initiation from persistent slip bands in polycrystals, Acta Materialia 59(1) (2011) 328-341.

[55] Y. Zhang, T.T. Zuo, Z. Tang, M.C. Gao, K.A. Dahmen, P.K. Liaw, Z.P. Lu, Microstructures and properties of high-entropy alloys, Progress in Materials Science 61 (2014) 1-93.

[56] W. Li, D. Xie, D. Li, Y. Zhang, Y. Gao, P.K. Liaw, Mechanical behavior of high-entropy alloys, Progress in Materials Science 118 (2021).

[57] T. Yang, Y.L. Zhao, Y. Tong, Z.B. Jiao, J. Wei, J.X. Cai, X.D. Han, D. Chen, A. Hu, J.J. Kai, K. Lu, Y. Liu, C.T. Liu, Multicomponent intermetallic nanoparticles and superb mechanical behaviors of complex alloys, Science 362(6417) (2018) 933-937.

[58] J. Su, D. Raabe, Z. Li, Hierarchical microstructure design to tune the mechanical behavior of an interstitial TRIP-TWIP high-entropy alloy, Acta Materialia 163 (2019) 40-54.

[59] J. Su, X. Wu, D. Raabe, Z. Li, Deformation-driven bidirectional transformation promotes bulk nanostructure formation in a metastable interstitial high entropy alloy, Acta Materialia 167 (2019) 23-39.

[60] I. Gutierrez-Urrutia, D. Raabe, Dislocation and twin substructure evolution during strain hardening of an Fe–22wt.% Mn–0.6wt.% C TWIP steel observed by electron channeling contrast imaging, Acta Materialia 59(16) (2011) 6449-6462.

[61] S. Fu, H. Bei, Y. Chen, T.K. Liu, D. Yu, K. An, Deformation mechanisms and work-hardening behavior of transformation-induced plasticity high entropy alloys by in -situ neutron diffraction, Materials Research Letters 6(11) (2018) 620-626.

[62] Z. Li, C.C. Tasan, H. Springer, B. Gault, D. Raabe, Interstitial atoms enable joint twinning and transformation induced plasticity in strong and ductile high-entropy alloys, Scientific reports 7 (2017) 40704.

[63] M. Wang, Z. Li, D. Raabe, In-situ SEM observation of phase transformation and twinning mechanisms in an interstitial high-entropy alloy, Acta Materialia 147 (2018) 236-246.

[64] C.-S. Yoo, Y.-M. Park, Y.-S. Jung, Y.-K. Lee, Effect of grain size on transformation-induced plasticity in an ultrafine-grained metastable austenitic steel, Scripta Materialia 59(1) (2008) 71-74.

[65] S. Mahajan, M.L. Green, D. Brasen, A model for the FCC→HCP transformation, its applications, and experimental evidence, Metallurgical Transactions A 8(2) (1977) 283-293.

[66] S.L. Wong, M. Madivala, U. Prahl, F. Roters, D. Raabe, A crystal plasticity model for twinning- and transformation-induced plasticity, Acta Materialia 118 (2016) 140-151.

[67] I. Gutierrez-Urrutia, S. Zaefferer, D. Raabe, The effect of grain size and grain orientation on deformation twinning in a Fe–22wt.% Mn–0.6wt.% C TWIP steel, Materials Science and Engineering: A 527(15) (2010) 3552-3560.

[68] Y. Liu, H. Yang, G. Tan, S. Miyazaki, B. Jiang, Y. Liu, Stress-induced FCC ↔ HCP martensitic transformation in CoNi, Journal of Alloys and Compounds 368(1-2) (2004) 157-163.

[69] M.F. Ashby, D. CEBON, Materials selection in mechanical design, Le Journal de Physique IV 3(C7) (1993) C7-1-C7-9.

[70] S. Rajasekhara, L. Karjalainen, A. Kyröläinen, P. Ferreira, Development of stainless steels with superior mechanical properties: a correlation between structure and properties in nanoscale/sub-micron grained austenitic stainless steel, Advanced Steels, Springer2011, pp. 371-384.

[71] G. Welsch, R. Boyer, E. Collings, Materials properties handbook: titanium alloys, ASM international1993.

[72] J.Y. He, H. Wang, H.L. Huang, X.D. Xu, M.W. Chen, Y. Wu, X.J. Liu, T.G. Nieh, K. An, Z.P. Lu, A precipitation-hardened high-entropy alloy with outstanding tensile properties, Acta Materialia 102 (2016) 187-196.

[73] W.H. Liu, Z.P. Lu, J.Y. He, J.H. Luan, Z.J. Wang, B. Liu, Y. Liu, M.W. Chen, C.T. Liu, Ductile CoCrFeNiMox high entropy alloys strengthened by hard intermetallic phases, Acta Materialia 116 (2016) 332-342.

[74] Y. Guo, M. Li, P. Li, C. Chen, Q. Zhan, Y. Chang, Y. Zhang, Microstructure and mechanical properties of oxide dispersion strengthened FeCoNi concentrated solid solution alloys, Journal of Alloys and Compounds 820 (2020).

[75] Y. Chen, H.W. Deng, Z.M. Xie, M.M. Wang, J.F. Yang, T. Zhang, Y. Xiong, R. Liu, X.P. Wang, Q.F. Fang, C.S. Liu, Tailoring microstructures and tensile properties of a precipitation-strengthened (FeCoNi)94Ti6 medium-entropy alloy, Journal of Alloys and Compounds 828 (2020).

[76] A. Fu, B. Liu, S. Xu, J. Huang, Y. Zhang, Y. Cao, Y. Liu, Mechanical properties and microstructural evolution of a novel (FeCoNi)86.93Al6.17Ti6.9 medium entropy alloy fabricated via powder metallurgy technique, Journal of Alloys and Compounds 860 (2021).

[77] S. Jiang, H. Wang, Y. Wu, X. Liu, H. Chen, M. Yao, B. Gault, D. Ponge, D. Raabe, A. Hirata, M. Chen, Y. Wang, Z. Lu, Ultrastrong steel via minimal lattice misfit and high-density nanoprecipitation, Nature 544(7651) (2017) 460-464.

[78] E.P. George, C.T. Liu, D.P. Pope, Fracture in Ni3Al: Environmental and Dopant Effects, physica status solidi (a) 160(2) (1997) 517-529.

[79] Z. Wu, H. Bei, G.M. Pharr, E.P. George, Temperature dependence of the mechanical properties of equiatomic solid solution alloys with face-centered cubic crystal structures, Acta Materialia 81 (2014) 428-441.

VITA

Zongyang Lyu was born in Linyi, China. He obtained a Bachelor of Science degree from the Department of Materials Science and Engineering at Shandong Jianzhu University in 2012. He earned his Master of Science degree at the Department of Materials Science and Engineering at University of Science & Technology, Beijing in 2016. In spring of 2017, he joined Dr. Peter Liaw group at The University of Tennessee, Knoxville to pursue his Ph.D. degree in materials science and engineering. He received a Doctor of Philosophy degree in May 2023.